CHALMERS

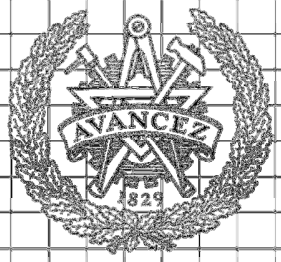

Sand erosion in dilute and dense mixtures

An Eulerian and Lagrangian CFD-study of wear correlations

Master of Science Thesis

OSCAR GRANBERG
MARTIN HÜBERT

Department of Applied Mechanical Engineering
Division of Fluid dynamics
CHALMERS UNIVERSITY OF TECHNOLOGY
Gothenburg, Sweden, 2012
Report No. xxxx

Abstract

Sand erosion is the cause of widespread structural damage in offshore pipe systems and it is often associated with large costs. Correlative and empirical methods are often used to predict erosion rates. Such procedures, however, tend to yield overly conservative estimates. In this thesis, a Lagrangian CFD model has been compared with some of the main correlative methods for predicting erosion in gas streams for pipe bends and blinded tees. It is found that the correlative methods differ by several orders of magnitude. The DNV RP O501 correlation under-predicts erosion by more than one order of magnitude for low density fluid mixtures at velocities below 10 m/s. Maximum erosion rates are obtained at intermediate sand particle diameters both for the pipe bend and blinded tee.

Furthermore, an Eulerian model for high particle loadings, derived for use in fluidized-bed combustors, has been adapted to predict erosion on steel grades. The model reproduces similar erosion patterns, as well as velocity and particle diameter dependencies, as correlative methods suggest. The magnitude of erosion has not been reproduced, presumably due to an erroneous proportionality constant. Eulerian methods are associated with inherent losses of vital information, such as the particle impingement angle and impact phenomena. We believe that the outlook is generally poor for accurate wear predictions in the Eulerian framework and capturing of effects such as lowered erosion efficiency in dense mixtures.

Acknowledgement

We would like to thank our supervisor at EDRmedeso, Klas Johansson, for the opportunity to carry out this master thesis. We would also like to thank our supervisor and examiner at Chalmers, associate professor Srdjan Sasic, for his inputs and assistance.

Table of contents

1. Introduction

1.1 Background

Wear is the process by which material and equipment degrade via material displacement. Wearing phenomena can be subdivided into different classifications depending on the mechanism by which the wear process occurs. Erosion, the main mechanism of interest in this treatise, is the mechanism by which material is removed by impinging particles via cutting or deforming action associated with short duration sliding contacts.

Offshore industry tackles severe erosion problems when trying to pump oil and gas from the seabed and transport it through pipe systems due to entailed sand, often in high concentrations. Damage caused by sand erosion is often associated with large costs due to maintenance problems at great depths, loss of production or environmental damage associated with structural failure. Therefore a great incentive lies in developing methods for combating wear processes. The first step in such a method is the accurate prediction of erosive wear rates. Erosion as a phenomenon has been studied and known for a very long time. In 1873 Reynolds released a paper on sandblasting, the first paper focusing on erosion. At the beginning of the 20th century technical papers treating erosion started to appear even though the understanding of the process wasn't that extensive. It was first when Iain Finnie released his landmark report in 1960 that the understanding of sand erosion reached such a level that the process could be accurately modeled [1]. Finnie based his model on a cutting analogy and could, based on assumptions of the ratio between forces and how the cutting process progressed, derive an expression for the volume of material removed. The volume of material removed was denoted Q and depended upon the mass of a single grain, m, the impact velocity V and impact angle α, Eq. (1).

$$Q = \frac{mV^2}{p\psi K}\left(\sin 2\alpha - \frac{6}{K}\sin^2\alpha\right),\ \tan\alpha \leq \frac{K}{6} \quad (1)$$

$$Q = \frac{mV^2}{p\psi K}\left(\frac{Kcos^2\,\alpha}{6}\right),\ \tan\alpha \geq \frac{K}{6} \quad (2)$$

The rate equations thus represented the fraction of particle kinetic energy which was converted to erosive wear. The fraction depends on impingement angle etc. Despite Finnie's landmark contribution, he failed to account for the fact that the velocity dependence often is higher than his predicted quadratic form. Moreover (2) predicts that there should be no erosion at all when particles impinge at close to normal incidence. A vast number of other proposed formulas of empirical and theoretical nature have emerged since Finnie's formula with similar functional dependencies. Notable contributions have been made by e.g. Bitter and his combined brittle and ductile model which accounts for important concepts such as energy dissipation and threshold velocity, the velocity above which erosion occurs [2], [3]. In the experiments conducted in the early period the particle incidence velocity was considered equal to the particle impact velocity and therefore, e.g. the equations proposed by Finnie were correlated, not with the particle velocity, but with the velocity of the free stream jet [4]. Laitone later proposed another

explanation for the higher velocity exponent [5]. From measurements he could conclude that the incident particles were accelerated faster than the average fluid free stream velocity of particle laden jets and could therefore grasp the need for CFD.

Due to the strong effect of fluid dynamics upon erosion rates, many of the published articles during the last two decades have focused on coupling between the two concepts. As described previously for lower values of the momentum equilibration number particles become entailed in eddies and change direction due to boundary layers etc. Therefore recent success in modeling can be attributed to a sequential procedure where Lagrangian particle trajectories, impingement angles and velocities are calculated using CFD. Thereafter by application of single particle erosion equations, often on the form given in eq. (3) such as Finnie's, on the obtained velocity and angle distribution, one can obtain detailed erosion predictions by summation over many such collisions events.

$$E_L = k \cdot m \cdot V^n \cdot f(\alpha) \tag{3}$$

Furthermore, more accurate empirical models can be obtained by coupling of experimental erosion results with the velocity and angle distributions [6], [7], [8], [9]. The angular dependency $f(\alpha)$ and the velocity exponent n, or even an arbitrarily chosen velocity function $g(v)$, can be determined by detailed CFD simulations of the experimental apparatus used, obtaining an erosive wear map. Then by e.g. a least square minimization procedure the functional dependence between the erosion rate and angle-velocity distribution can be determined. Even if this procedure lacks the potential of complete generality, promising predictive ability modeling other geometries have been observed.

With the rise of fluidized bed combustors (FBC), erosion in dense multiphase mixtures became a large problem. This necessitated the need for simulation tools applicable at such conditions. Due to the large costs associated with simulations in the Lagrangian framework of dense mixtures, effort has been directed towards the development of two fluid models for prediction of erosion. The most widely used method for this has been the monolayer energy dissipation (MED) model [10], [11], [12], [13], suggested by Bouillard and Lyczkowski in 1987 [14]. The model is an extension from the power dissipation erosion model for low impingement angle erosion proposed by Ushimaru in 1984 [15]. The model is based on dissipation of mechanical energy by several mechanisms, erosion being one of them. Energy can also be dissipated into heat or in attrition processes. In addition to the MED model Lyczkowski derived another erosion model for dense mixtures together with Ding by fusion of Finnie's equations with kinetic theory of granular flow (KTGF) [16]. The total erosion rate was obtained by integration of Finnie's equation over all particle impact velocities. The result of integration is presented in Eq. (4).

$$\dot{E} = 2\epsilon_s \rho_d \frac{1}{8p}\left[\frac{1}{10}\frac{(2T)^{2/3}}{\sqrt{\pi}} + \frac{1}{10}\frac{v_{w-t}^2}{2}\sqrt{\frac{2T}{\pi}} + \frac{9}{100}v_{w-t}T\right] \tag{4}$$

However most sand erosion predictions in the offshore industry have been carried out with far less complex methods consisting of a range of correlative methods. These have been shown to give markedly different results applied to the same situation as well as being overly conservative, overestimating wear rates. There is therefore a great incentive to evaluate and compare often used correlations with CFD-simulations as well as evaluate the effect of dense sand flows upon erosive wear.

1.2 Objective

The goal of this thesis is to evaluate an Eulerian model for prediction of sand erosion in dense mixtures. The aim is to investigate whether or not the model can be used for wear predictions in pipe components such as blinded tees and elbows. Furthermore a Lagrangian model will be implemented and used to infer the effect upon erosion for various parameters such as flow velocity, pipe diameter, type of fluid, and particle diameter. The results will be evaluated and compared with some of the main correlative methods for wear predictions available to industry. The expected outcome of this study was to obtain sufficient information about the Eulerian model to make a statement of its applicability. Furthermore we wished to investigate the accuracy of industrial correlations as compared to CFD-simulations and infer particle, geometry and flow variable dependency for the erosion process.

1.3 Limitations

Simulations were only carried out in two specific geometries, the pipe bend and the blinded tee. They are two of the most wear prone components in pipe systems.

All simulations were done in particle laden gas streams such as methane and air streams. Gas streams require less simulation time and erosion in such systems are much larger than in liquids. Most systems facing sand erosion, such as offshore piping systems are exerted to mixtures of both gas and liquid. Predictions of erosion rates in gas are therefore relevant, also to such systems.

Correlative methods used for comparison was limited to the correlation presented by Det Norske Veritas (DNV) report DNV RP O501 from the work of Kvernvold [17] and the alternative to API RP 14E proposed by Salama [18]. Furthermore comparisons and comments are made with correlations proposed by Venkatesh et al. and Arnold e. al.

2. Theory

2.1 Wear correlations

There are four main correlative methods in use by the industry for sand erosive wear predictions applicable to standard pipe components such as pipe bends and blinded tees. These are the works by Salama and Venkatesh, Kvernvold for Det Norske Veritas (DNV), Shirazi et al. of Tulsa University and Lockett et al. of AEA. The DNV model and the model developed at Tulsa University both try to account for fluid dynamical effects resulting in deviating particle trajectories. The AEA and Salama and Venkatesh models lack this capability and therefore only handle pure gas flows. The AEA model is based solely on empirical correlation and uses a group of parameters, x, y and z, with a functional dependency upon v_s, the superficial gas velocity, together with the parameter A, comprised of groups of fluid and flow variables, Eq. (5).

$$E_{AEA} = J \cdot (b_1 U_p^n + b_2 \cdot e^{-b3 \cdot U_p}) \quad (5)$$

The Salama and Venkatesh model is similar to Finnie's expression but also accounts for the effect of changing pipe diameter. The model is applicable to pipe bends and blinded tees. The angular dependency is set to one, overestimating erosion at small impact angles. The proportionality constant is derived from experiments, Eq. (6).

$$E = K \cdot \frac{W_s \cdot V^2}{D^2} \quad (6)$$

Where K is a proportionality constant, W is sand flow rate in lb/day, V is fluid flow velocity in ft/s, D is the internal pipe diameter in inches yielding the erosion, E, in milliinches/year. In addition to the proposed values of K by Salama, Arnold and Svedeman proposed less conservative values.

As mentioned earlier the DNV model takes fluid dynamical effects into account when predicting sand erosion. For the pipe bend e.g. the curvature is taken into account through the impact angle, α. Particle size effects are accounted for via G the particle size correction factor and C_1 the geometry factor. These variables act as modifiers to Finnie´s expression resulting in the form given by Eq. (7).

$$\dot{E_L} = \frac{\dot{m}_p \cdot K \cdot F(\alpha) \cdot \sin(\alpha) \cdot U_p^n}{\rho_t \cdot A_{pipe}} G \cdot C_1 \cdot C_{unit} \quad (7)$$

The expression for the blinded tee is similar to the pipe bend expression except for the neglected angular dependency, Eq. (8).

$$\dot{E_L} = \frac{\dot{m}_p \cdot K \cdot U_p^n}{\rho_t \cdot A_t} G \cdot C_1 \cdot C_{unit} \quad (8)$$

The calculation of the modifying constants for the blinded tee is carried out in two ways depending on the quota between particle and fluid density. The cut off between the two paths of

calculation is where increasing particle size no longer results in larger outlet erosion while particles tend to deviate completely from streamlines impacting the blinded section of the blinded tee.

The University of Tulsa model also uses a variant of Finnie's erosion model. Albeit with a much smaller velocity exponent of only 1.73.

2.2 Eulerian-Lagrangian methods

The Eulerian-Lagrangian approach has been the cornerstone for erosive wear predictions in academic settings since computational fluid dynamics emerged, due to its conceptually simple extension from single particle wear equations. The single particle wear equations such as the Finnie erosion model predicts the material loss associated with a one-particle collision event. The material loss generally depends upon the material hardness as well as the mass, size, velocity and impact angle of the particle. In the Eulerian-Lagrangian approach this material loss associated with one impact is summed up for a large number of particle impacts over the surfaces of interest. Information of particle mass, size, velocity and impact angle are obtained from the interaction of particles with the continuous flow field. In this section the equations governing this method are described as well as adaptations made in order to fuse the fundamental theory with the commercial CFD code ANSYS Fluent 14.0

2.2.1 Continuous phase equations

2.2.1.1 Conservation of mass and momentum

The equations governing the continuous phase flow are the conservation equations for momentum and mass, formally known as the continuity equation (9) and the Navier-Stokes equation (10).

$$\nabla \cdot (\rho \vec{v}) = 0 \tag{9}$$

$$\nabla \cdot (\rho \vec{v}\vec{v}) = -\nabla p + \nabla \cdot (\bar{\bar{\tau}}) + \vec{F} \tag{10}$$

Where the stress tensor $\bar{\bar{\tau}}$ is a function of strain rates and for compressible flows also dilatational effects, Eq. (11).

$$\bar{\bar{\tau}} = \mu\left[(\nabla \vec{v} + \nabla \vec{v}^{T}) - \frac{2}{3}\nabla \cdot \vec{v} I\right] \tag{11}$$

These equations are for numerical reasons transformed to the Reynolds averaged Navier-Stoke equations (RANS) via the Reynolds decomposition by assuming that the instantaneous velocities can be decomposed into an averaged flow field velocity with an added fluctuating component, $\vec{v} = \bar{\vec{v}} + \vec{v}'$. Thereafter this expression is substituted for the velocities in (10) and the RANS equations (12) are obtained after averaging.

$$\rho \bar{v}_j \frac{\delta \bar{v}_i}{\delta x_j} = \rho \bar{f}_i + \frac{\delta}{\delta x_j}\left[-\bar{p}\delta_{ij} + \mu_m\left(\frac{\delta \bar{v}_i}{\delta x_j} + \frac{\delta \bar{v}_j}{\delta x_i}\right) - \rho\overline{u_i' u_j'}\right] \tag{12}$$

This however leads to the closure problem due to the Reynolds stresses, $\rho\overline{u_i' u_j'}$, which emerges after averaging. One strategy is to model the Reynolds stresses via the Boussinesq approximation assuming an eddy viscosity as an analogy to the ordinary stress strain relation for viscous flows, Eq. (13).

$$\rho\overline{u_i' u_j'} = -\rho\nu_t\left(\frac{\delta\bar{v}_i}{\delta x_j} + \frac{\delta\bar{v}_j}{\delta x_i}\right) + \frac{2}{3}\left(\rho \cdot k + \nu_t \frac{\delta\bar{v}_k}{\delta x_k}\right)\delta_{ij} \tag{13}$$

This approach however has introduced the eddy viscosity ν_t which needs to be modeled. This can be done via one of the two equation models for turbulence such as the $k-\epsilon$ model.

2.2.1.2 Turbulence modeling

Throughout this thesis two turbulence models have been utilized, the $k-\epsilon$ and the shear stress transport (SST) formulation of the $k-\omega$ model. In this section the $k-\epsilon$ model will be described in some detail the SST model will be described in section 2.3.1.5. The $k-\epsilon$ model uses two transport equations for turbulent kinetic energy k, and energy dissipation ϵ. The length scale of turbulence is stored in the dissipative variable and k is a measure of turbulent energy. The formulation of the k transport equation used contains a generation term due to the production from mean gradients, G_k. However effects such as buoyancy and fluctuating dilatation in compressible turbulence have been neglected resulting in equation (14).

$$\frac{\partial}{\partial x_i}(\rho k u_i) = \frac{\partial}{\partial x_j}\left[\left(\mu + \frac{\mu_t}{\sigma_k}\right)\frac{\partial k}{\partial x_j}\right] + G_k - \rho\epsilon \tag{14}$$

$$G_k = \mu_t 2 S_{ij} S_{ij} \tag{15}$$

$$S_{ij} = \frac{1}{2}\left(\frac{\partial u_j}{\partial x_i} + \frac{\partial u_i}{\partial x_j}\right) \tag{16}$$

The transport equation for the dissipative energy contains source terms for generation and dissipation of the dissipative variable, Eq. (17).

$$\frac{\partial}{\partial x_i}(\rho\epsilon u_i) = \frac{\partial}{\partial x_j}\left[\left(\mu + \frac{\mu_t}{\sigma_\epsilon}\right)\frac{\partial\epsilon}{\partial x_j}\right] + C_{1\epsilon}\frac{\epsilon}{k}G_k - C_{2\epsilon}\rho\frac{\epsilon^2}{k} \tag{17}$$

From these variables the eddy viscosity in the Boussinesq approximation can then be calculated eq. (18).

$$\mu_t = \rho C_\mu \frac{k^2}{\epsilon} \tag{18}$$

The modeling constants are experimentally derived and given below.

$$C_{1\epsilon} = 1.44, C_{2\epsilon} = 1.92, C_\mu = 0.09, \sigma_k = 1.0, \sigma_\epsilon = 1.3 \tag{19}$$

2.2.1.3 Boundary conditions

The boundary conditions used solving the momentum equations were fixed velocity at the inlet, no-slip at walls and the standard outflow condition at the outlet. For turbulence the turbulent energy and dissipation were fixed at the inlet and no transport normal to walls were allowed, standard outflow conditions were set at the outlet.

2.2.2 Discrete phase equations

A modified version of the classical BBO (Basset-Boussinesq-Oseen) formulation of Newton's second law of motion is utilized to simulate the particle trajectories. The forces affecting the particle during simulation were considered limited to drag, Eq. (20).

$$\frac{d\vec{u}_p}{dt} = F_D(\vec{u} - \vec{u}_p) \tag{20}$$

$$F_D = \frac{18\mu_m}{\rho_p d_p^2}\frac{C_D Re}{24} \tag{21}$$

Drag was modeled by the spherical drag law proposed by Alexander and Morsi given in Eq. (22). The model constants used depend upon the Reynolds number.

$$C_D = a_1 + \frac{a_2}{Re} + \frac{a_3}{Re^2} \tag{22}$$

While the governing equations for fluid motion only resolves the average flow field, turbulent effects upon particle movement have to be modeled. This can be done via the so called discrete random walk model. Here the effects of eddies are simulated via sampling of a fluctuating velocity component, $u = \bar{u} + u'$ which is a function of turbulent kinetic energy and a Gaussian random variable, Eq. (23).

$$u' = \zeta\sqrt{\frac{2k}{3}} \tag{23}$$

The fluctuation velocity vector is then held constant for a period of time until another vector is sampled. By assuming small tracer particles i.e. particles with zero drift, the Lagrangian timescale can be used as the integral time scale used between samplings according to Eq. (24).

$$\tau_e = 2T_L \tag{24}$$

The Lagrangian time scale can be estimated from the turbulent energy and length scale.

$$T_L = C_L\frac{k}{\varepsilon} \tag{25}$$

$$C_L = 0.15 \tag{26}$$

The irregularity of sand grains and their inhomogeneous composition together with different material characteristics of the impacted surface leads to deviations compared to spherical

partially elastic bodies impacting an ideal surface. Many erosive wear studies have used constant restitution coefficients, however polynomial expansions of the impingement angle have been proposed in the literature based on both theoretical and experimental considerations. Tabakoff and Sommerfeld showed the sensitivity of restitution to impact angle and proposed a stochastic method for sampling restitution coefficients from a mean and standard deviation derived from experimental measurement, see Eq. (27).

$$e_{tan} = 0.993 - 1.76\alpha + 1.56\alpha^2 - 0.49\alpha^3$$

$$e_{norm} = 0.998 - 1.66\,\alpha + 2.11\,\alpha^2 - 0.67\,\alpha^3 \quad (27)$$

$$\sigma_{tan} = -0.0005 + 0.62\alpha - 0.535\alpha^2 + 0.089\alpha^3;$$

$$\sigma_{norm} = 2.15\alpha - 5.02\alpha^2 + 4.05\alpha^3 - 1.085\alpha^4$$

However due to the strong dependence upon the impacted material relations are needed for steel grades. Froder et al. proposed a set of equations for the normal and tangential restitution based on experiments conducted as Southhampton university at AISI 4130 steel. These are markedly different from constant restitution coefficients, see Eq. (28).

$$\begin{aligned} e_{norm} &= 0.988 - 0.78\alpha + 0.19\alpha^2 - 0.024\alpha^3 + 0.027\alpha^4 \\ e_{tan} &= 1 - 0.78\alpha + 0.84\alpha^2 - 0.21\alpha^3 + 0.028\alpha^4 - 0.022\alpha^5 \end{aligned} \quad (28)$$

2.2.3 Wear predictive equations in the E-L framework

The functional form of the erosion equation used throughout all simulations in this thesis are based upon Finnies original one-particle formulation but the constants used are not strict material properties, such as the Vickers hardness, but the experimentally derived constants of Kvernvold. The removed material is dependent upon particle mass, velocity, impact angle and the hardness of the eroded material, Eq. (29).

$$E = Km_p|\overrightarrow{U_P}|^n f(\alpha) \quad (29)$$

The material hardness governs the size of the proportionality constant K. The dependency upon impact angle is described by $f(\alpha)$. Usually the functional dependence is trigonometric in nature if derived from fundamental concepts, but for our purposes a polynomial expansion is used, Eq. (30).

$$f(\alpha) = \sum_{i=1}^{8}(-1)^{i+1}A_i\left(\frac{\pi\alpha}{180}\right)^i \quad (30)$$

$$A_i \in \{9.370\ \ 42.295\ \ 110.864\ \ 175.804\ \ 170.137\ \ 98.398\ \ 31.211\ \ 4.170\}$$

Constants for various materials can be found in Kvernvold.

2.2.4 Adaptation to ANSYS Fluent 14.0

Fluent has support for wear calculations for discrete particle models and the form described in section 2.2.3 can be implemented in the graphical user interface with one exception. The polynomials must be on the form $f(\alpha) = \sum_{i=0}^{7} a_i \alpha^i$ therefore a least square adaptation of the polynomial described in 2.2.3 was carried out in order for the implementation to work. The coefficients obtained are given below.

$$a_i \in \{0.004474 \;\; 8.9543 \;\; -36.906 \;\; 84.0549 \;\; -109.68 \;\; 81.01373 \;\; -31.56217 \;\; 5.041349\}$$

2.3 Eulerian-Eulerian methods

In the Eulerian-Eulerian framework all phases including the dispersed phase are viewed as continuous and are modeled as such. In this thesis kinetic theory of granular flow (KTGF) has been utilized to describe the dispersed phase and the erosive wear process. The following sections give a brief outline of the equations used and the adaptations done to implement them into the Fluent code.

2.3.1 Continuous phase equations

2.3.1.1 Conservation equations

The solid phase is assumed to consist of hard, spherical and smooth particles undergoing binary collisions. Furthermore the particles are assumed to be of uniform density and size. Therefore the underlying assumptions for the Boltzmann equation holds and by assuming that the particle velocity distribution is Maxwellian the transport equation for the solid phase can be closed. Furthermore one assumes that the Enskog assumption for the pair-distribution holds and that the pre-collisional velocities are uncorrelated for colliding particles. The gas phase is assumed Newtonian which leads us to the conservation equations for mass and momentum used throughout the Eulerian-Eulerian simulations.

$$\frac{\delta}{\delta t}(\alpha_i \rho_i) + \nabla \cdot (\alpha_i \rho_i \vec{v}_i) = 0, \quad i = 1,2 \tag{31}$$

$$\sum \alpha_i = 1 \tag{32}$$

Source terms such as interphase mass transfer have been neglected. The momentum balance for phase i yields the following expression (33).

$$\frac{\partial}{\partial t}(\alpha_i \rho_i \vec{v}_i) + \nabla \cdot (\alpha_i \rho_i \vec{v}_i \vec{v}_i) = -\alpha_i \nabla P + \nabla \cdot \bar{\tau}_i + \alpha_i \rho_i \vec{g} + K_{ij}(\vec{v}_i - \vec{v}_j) \tag{33}$$

$$\bar{\tau}_i = \alpha_i \mu_i \left(\nabla \vec{v}_q + \nabla \vec{v}_q^T\right) + \alpha_i \left(\lambda_i - \frac{2}{3}\mu_i\right) \nabla \cdot \vec{v}_q \bar{I} \tag{34}$$

2.3.1.2 Momentum exchange coefficient

The secondary solids phase is assumed to consist of spherical, smooth particles. Therefore the Schiller and Neumann drag formula was used to estimate the interphase drag, Eq. (35). The solid phase is hereafter denoted s.

$$K_{is} = \frac{\alpha_i \alpha_s \rho_s f}{\tau_s} \tag{35}$$

τ_s is the particle relaxation time and f is the interphase drag function.

$$\tau_s = \frac{\rho_s d_p^2}{18\mu_m} \tag{36}$$

$$f = \frac{C_D Re}{24} \tag{37}$$

$$C_D = \begin{cases} 24(1 + 0.15Re^{0.687})/Re & Re \leq 1000 \\ 0.44 & Re > 1000 \end{cases} \tag{38}$$

2.3.1.2 Solids pressure

The solids pressure accounts for the energy transfer in the granular phase and is used in the granular phase momentum equation. It is composed of two parts, one accounting for kinetic motion and one for particle-particle collisions. Lun et al. proposed the following expression for the solid pressure, Eq. (39).

$$p_s = \rho_s \alpha_s T[1 + 2(1 + e_{ss}) g_0 \alpha_s] \tag{39}$$

T is the granular temperature described in section 2.3.14, e_{ss} the restitution coefficient for particle-particle collisions and g_0 the radial distribution function which is related to dimensionless distance between particles.

$$g_o = \frac{3}{5}\left[1 - \left(\frac{\alpha_s}{\alpha_{s,max}}\right)^{1/3}\right]^{-1} \tag{40}$$

2.3.1.3 Solids shear stresses

The shear stresses are modeled via an analogy to the stress-strain relation of Newtonian fluids. The solids viscosity is assumed to consist of a kinetic and a collisional contribution, Eq. (41).

$$\mu_s = \mu_{s,kin} + \mu_{s,col} \tag{41}$$

The expression suggested by Syamlal et al, Eq. (36), was used for the kinetic contribution and Gidaspow et al. for the collisional contribution, Eq. (42).

$$\mu_{s,kin} = \frac{\alpha_s d_s \rho_s \sqrt{T\pi}}{6(3 - e_{ss})}\left[1 + \frac{2}{5}(1 + e_{ss})(3e_{ss} - 1)\alpha_s g_0\right] \tag{42}$$

$$\mu_{s,col} = \frac{4}{5}\alpha_s^2 d_s \rho_s g_0 (1 + e_{ss})\sqrt{\frac{T}{\pi}} \quad (43)$$

2.3.1.4 Granular temperature

The granular temperature used to estimate solid shear stresses is a measure of the fluctuating particle velocities which is a measure of the energy content of the solid phase. Due to the analogy of kinetic gas theory the granular temperature can be modeled via a partial differential equation by which the granular temperature is convected and conducted, Eq. (44).

$$\frac{3}{2}\left[\frac{\partial}{\partial t}(\alpha_s \rho_s T) + \frac{\partial}{\partial x_i}\left(\alpha_s \rho_s \vec{v}_{s,i} T\right)\right] = \left[-p_s \delta_{ij} + \tau_{s,ij}\right]\frac{\partial \vec{v}_{s,i}}{\partial x_j} - \frac{\partial}{\partial x_i}\left(\kappa \frac{\partial T}{\partial x_i}\right) - \gamma \quad (44)$$

The expression of Syamlal et al. was used for the granular conductivity and is given in equation (45).

$$\kappa_T = \frac{15\alpha_s d_s \rho_s \sqrt{T\pi}}{4(41-33\eta)}\left[1 + \frac{12}{5}\eta^2(4\eta - 3)\alpha_s g_0 + \frac{16}{15\pi}(41 - 33\eta)\eta\alpha_s g_0\right] \quad (45)$$

Where $\eta = \frac{1}{2}(1 + e_{ss})$

2.3.1.5 Turbulence modeling

For all Eulerian-Eulerian simulations the $k - \omega$ shear stress transport SST formulation was used. The turbulence model employs the $k - \varepsilon$ transport equations in the far field and resolves the boundary layer with the $k - \omega$ model. A blending function being one in the boundary layer and zero in the far field controls which of the two sets of turbulence equations to be employed in any given region.

2.3.1.6 Boundary conditions

The difference compared to section 2.2.1.3 and the Eulerian-Lagrangian boundary conditions are the conditions set for the granular temperature, the volume fraction of the two phases, and the momentum condition for the granular phase. A fixed granular temperature was used at the inlet and the no flux condition was applied at walls. The volume fraction was also fixed at the inlet. A partial slip condition, Eq. (46), was applied at the walls according to ding et al.

$$v_{i|wall} = -\lambda_p \frac{\partial v_{i|wall}}{\partial n} \quad (46)$$

Where n is the wall normal direction.

$$\lambda_p = \frac{\sqrt{3\pi}}{24}\frac{d_p}{\alpha_s g_0} \quad (47)$$

2.3.3 Wear predictive equations in the E-E framework

All KTGF simulations throughout this thesis have implemented a modified version of the wear model developed by Lyczkowski et al. The wear model is an extension of Finnie's single particle model. Lyczkowski assumed a Maxwellian distribution of particle velocities and could therefore

sum up the contributions to the erosive wear for all particle velocities. In doing so one obtains the expressions for erosive wear in the KTGF framework, see Eq. (48). In section X the derivation procedure is covered in full detail as our variation of the Lyczkowski model is presented.

$$E_{tot} = 2\alpha_s\alpha_s B_F \left[\frac{(2T)^{3/2}}{10\sqrt{\pi}} + \frac{v_w^2}{20}\sqrt{\frac{2T}{\pi}} + \frac{9}{100}v_w T\right] \quad (48)$$

2.3.4 Adaptation to ANSYS Fluent 14.0

A partial slip boundary condition, as described in 2.3.1.6 is required when implementing the Lyczkowski model. Fluent has no GUI capabilities to handle the required boundary conditions and therefore a user defined function (UDF) has to be programmed in C and hooked to the solver routine of Fluent. In order to simultaneously terminate wall functions for velocity, the script had to be implemented via the specified shear condition.

This section describes schematically how this was done. Assume an orthonormal basis x′y′z′ centered at a boundary face. Let the face plane be a subdomain of the plane spanned by y′z′. The partial slip boundary condition, used by Lyczkowski, in three dimensions have two non-zero components, Eq. (49).

$$v_{i'} = -A\frac{dv_{i'}}{dz'}, i = 1,2 \quad (49)$$

Where

$$A = \frac{\sqrt{3\pi}}{24}\frac{d_p}{\alpha_s g_0} \quad (50)$$

The strain stress relation for an incompressible fluid at the boundary face is given by Eq. (51)

$$\tau_{z'i'} = -\mu_m S_{z'i'} = -\mu_m\left(\frac{dv_{i'}}{dz'} + \frac{dv_{z'}}{di'}\right), i = 1,2 \quad (51)$$

Assume that $dv_{z'}/di'$ component of the stress tensor always is much smaller than the $dv_{i'}/dz'$ component therefore resulting in Eq. (52).

$$\frac{\tau_{z'i'}}{\mu_m} = -\frac{dv_{i'}}{dz'} \quad (52)$$

Insertion into expression (49) results in the final form of the shear condition applied.

$$\tau_{z'i'} = v_{i'}\mu_m/A \quad (53)$$

$$\tau_{z'z'} = 0 \quad (54)$$

Details regarding the C-code and implementation are given in Appendix 1.

3. Method

3.1 Procedure

A literature survey was conducted in order to get an overview of the current state of research in the field of sand erosion. Over seventy articles and reports spanning from early 20th century to this date were found to be of significance. Thereafter geometries were constructed for three common pipe structures known to be prone to erosive wear and often used for investigations of sand erosion, the welded joint, the pipe bend, and the blinded tee. Eulerian-Lagrangian simulations were carried out on the geometries using an adaptation of Finnie's wear modeled as suggested by DNV RP O501. Parameter variations were carried out spanning over particle size, flow field velocity, type of fluid, geometry dimensions, choice of restitution coefficients and other simulation parameters such as discretization scheme, mesh refinement, particle sampling volume and choice of turbulence model. Simulation results were compared to the main industrial correlations used for prediction of sand erosion such as DNV RP 0501, Salama and Venkatesh's and Arnold's models. Furthermore the Eulerian-Lagrangian simulations were validated against a sand erosion experiment published by Wong et al.

Thereafter Eulerian-Eulerian simulations were carried out. Lyczkowski's model for wear prediction with kinetic theory of granular flow derived from Finnie´s model were slightly adjusted to conform with DNV RP 0501's suggested velocity exponent and coefficients. Thereafter user defined functions (UDFs) were written, facilitating the implementation of the erosion model into the CFD software, for details see section X. Furthermore a partial slip condition had to be modified and implemented as a UDF, see section X. Simulations were carried out focusing on erosion in pipe bends.

3.2 Summary of simulations

3.2.1 Geometry

As mentioned in the previous section three geometries were used throughout all simulations, the welded joint, the pipe bend and the blinded tee, see Fig. 1.

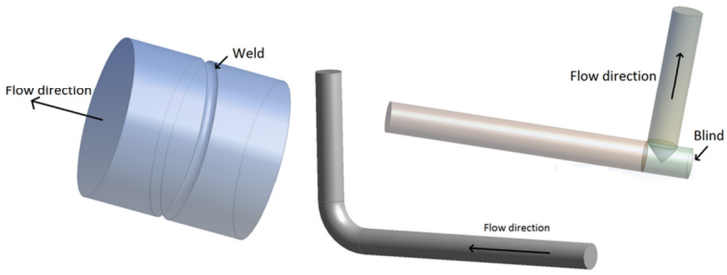

Fig. 1: Geometries under investigation; the welded joint, the pipe bend and the blinded tee.

Furthermore, for the replication of the experimental set by Wong et al., a pipe with a fixed plate with a centered hole was used. The geometry is depicted in Fig. 2.

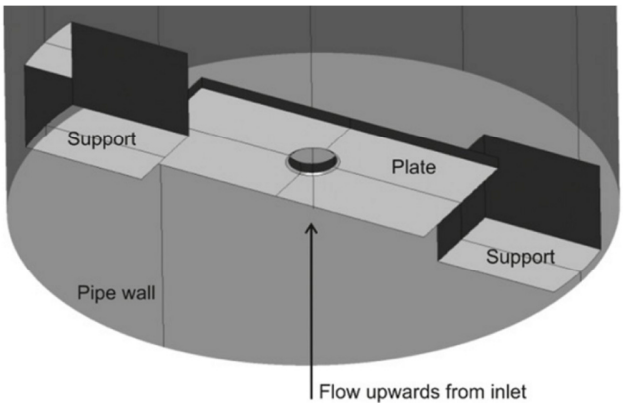

Fig. 2: Plate with hole through center point fixed via support at the inner pipe wall. Sand travelling through the pipe will impact plate and due to the hole in plate center deviate from straight trajectories before impact.

List summarizing dimensional characteristics for the pipe bend, the blinded tee, the welded joint, and the experimental setup can be found in appendix 5.

3.2.2 Case operating conditions

Simulations were primarily chosen such that relevant operating conditions for industrial settings would be replicated. Secondly limitations on flow velocity, loading etc had to be set due to excessive simulation cost. Constant mass sand flow rates were used when deducing particle size effects and flow velocity effects while constant particle loading were used investigating geometry dependence, while the question: "how much erosion will occur at this rate of production and sand loading?" is more relevant than that of changing particle loads with changing geometry. Details about case operating conditions can be found in Appendix U

3.2.3 Solver settings

Table 1 summarizes all ANSYS Fluent 14.0 solver settings utilized throughout simulations. Due to stability and convergence issues low order discretization had to be adopted for Eulerian simulations. UDFs where hooked to Fluent in order to implement the Eulerian erosion model as well as the partial slip boundary condition.

Table 1: Solver settings used in ANSYS Fluent 14.0 for all CFD-simulations.

	Lagrangian simulations	Eulerian simulations
Solver settings		
Type:	Pressure-based	Pressure-based
Velocity formulation:	Absolute	Absolute
Time setting:	Steady	Steady
Viscous model		
Model:	k-epsilon standard/realizable	k-omega SST
Near-Wall treatment	Standard Wall functions/Enhanced wall treatment	Per Phase
Boundary conditions		

Wall:	No-slip, Polynomial erosion model	1st phase: No-slip 2nd phase: Partial slip, no flux gt.
Inlet:	Fixed velocity, turbulent intensity and length scale	Fixed vel., turbulent intensity, length scale and gt.
Outlet:	Standard outflow conditions	Pressure outlet

Solution methods		
Scheme:	SIMPLE	Phase Coupled SIMPLE
Gradient approximation:	Least Squares Cell Based	Least Squares Cell Based
Momentum:	Second Order Upwind	Second order upwind
Turbulent kinetic energy:	Second Order Upwind	First order upwind
Turbulent dissipation Rate:	Second Order Upwind	Second First order upwind
Pressure:	Standard treatment	First order upwind
		First order upwind

Plane surface	Multiphase model
Bounded: on	Model: Eulerian
Sample points: on	Scheme: Implicit
Plane orientation: Aligned with inlet plane in all cases	

Discrete phase model	Secondary phase
Interaction with continuous phase: On	Granular temperature model: Partial differential equation
Max number of steps: >500	Phase material: Granular
Step length: 5	Granular Viscosity: Syamlal Obrien
Drag law: Spherical	Granular Bulk Viscosity: constant 0
Physical model accretion/erosion: On	Granular Conductivity: Syamlal Obrien
Accuracy Control: On	Solids Pressure: Lun-et-al
Tolerance: 1e-5	Radial distribution: Lun-et-al
Max Refinements: 20	Elasticity Modulus: Derived
Tracking Scheme Selection: Automated	Packing limit: 0.63
High Order Scheme: Trapezoidal	
Low Order Scheme: Implicit	
Injection type: Surface	
Turbulent dispersion: On	
Number of tries: >1000000 particles	

4. Results/discussion

4.1 Introduction to results

In the following section our simulation results will be presented, both in the Eulerian and Lagrangian framework. The results will be accompanied with our interpretation and comments closely related to specific results. Section 5 contains conclusions of more general nature. Appendix 4 and 5 can be consulted for detailed information about flow conditions and geometry dimensions.

4.2 Eulerian-Lagrangian

4.2.1 Independence of solver settings

Before commencing with simulation the particle-fluid interaction dependency upon wear rates were investigated. Simulations with both 1 and 2-way coupling were compared. Being able to neglect 2-way coupling decreases computational power by several orders of magnitude. No difference was found between 1-way and 2-way coupled cases. Due to the independency of particle interaction upon wear rates, 2-way coupling was neglected throughout all simulations.

Furthermore before every simulation it must be concluded whether or not the particle sampling size is sufficient to ensure statistically stable wear rates. The sampling size needed is a function of the overall complexity and size of the geometry. Meshing has a major impact on obtaining statistically stable rates where coarse meshes become stable for substantially less particles. On a fine mesh, “spotty” wear patterns are obtained when insufficient sampling has been done, caused by several particle impacts at certain faces while others have zero impacts. As a result one obtains much larger predicted maximum erosion rates than a sufficiently large sampling size would result in. In Fig. 3 and 4 the sampling size has been incrementally increased for the welded joint until an asymptotical behavior was observed.

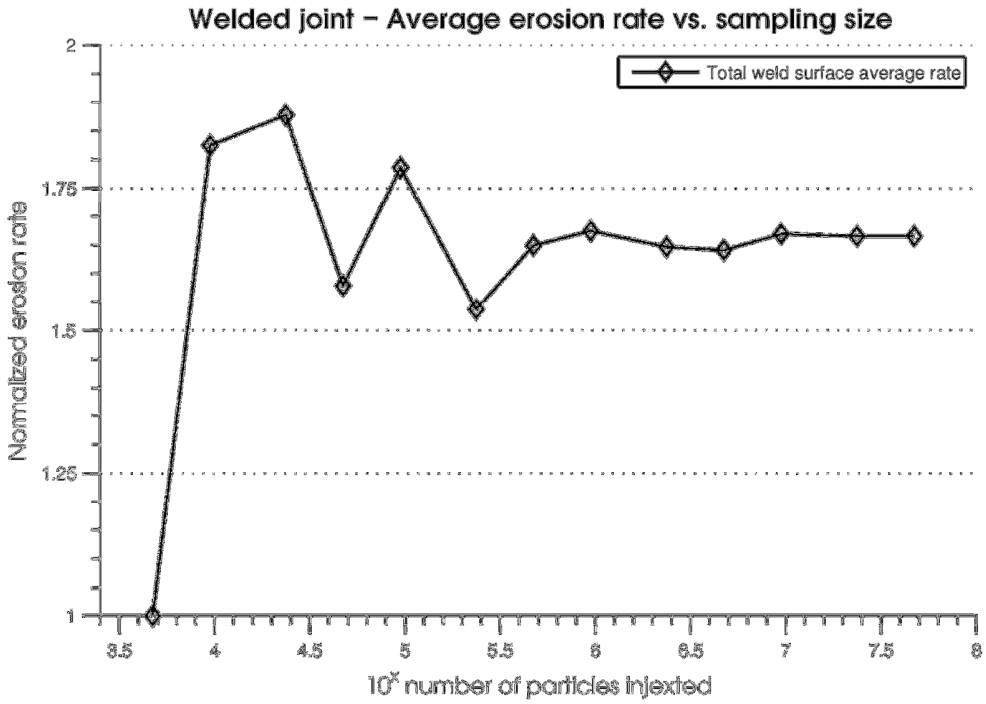

Fig 3: Incremental increase in sampling volume versus average erosion rate for a welded joint with a diameter of 0.1 m and a weld height of 2 mm.

The fluid is air and the flow velocity is 1 m/s. From the graphs one can see that the average wear rate of the entire weld reaches its asymptote for fewer particles than the maximum rate which requires substantially larger sampling volumes.

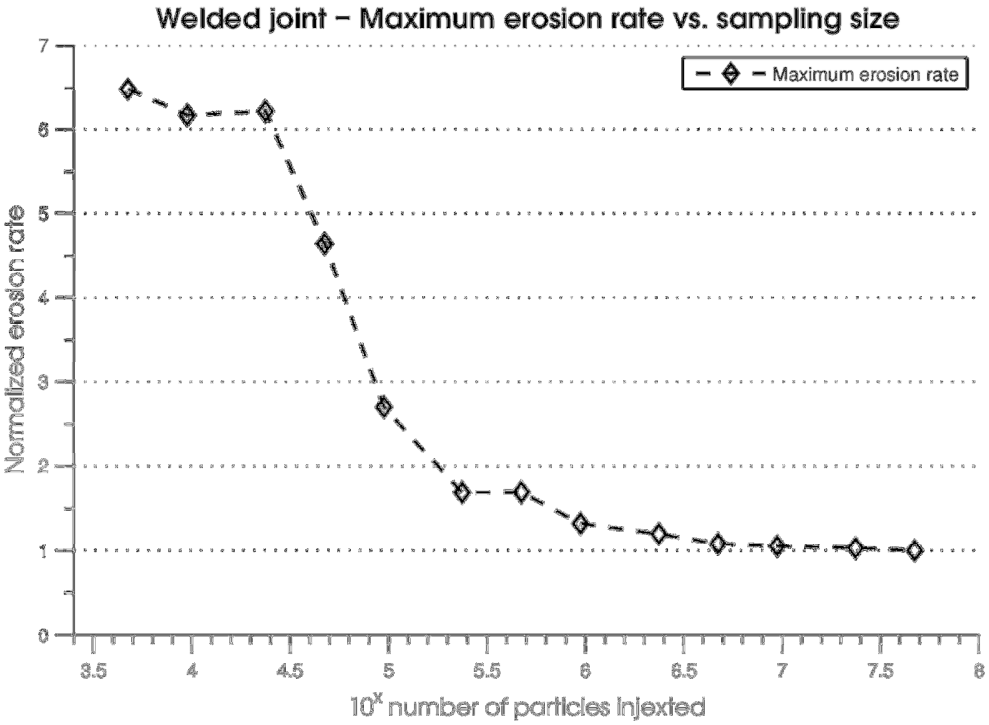

Fig 4: Incremental increase in sampling volume versus average erosion rate for a welded joint with a diameter of 0.1 m and a weld height of 2 mm.

4.2.2 Particle size

The effect of sand particle size upon erosion was deduced by a set of simulations covering the range of most sand types. Common sand distributions span a range of below 100 µm up to approximately 500 µm. Simulations were also carried out just outside this range to clarify the large scale trend, the total range of simulations spanned from 10 µm up to 1 mm. Two pipe configurations prone to erosive wear and therefore of industrial interest were focused upon, the blinded tee and the pipe bend. We chose to simulate one of the most wear causing flows in the oil industry, production of natural gas at different velocities from 1 m/s up to 50 m/s. The natural gas was modeled as pure methane at 7 bar and 373 K.

Erosion in the pipe bend was sampled at the point of maximum erosion and as a profile spanning the whole bend through the center plane as depicted by the highlighted field in Fig. 5. Maximum erosion rates were sampled for the blinded tee at the far wall of the outlet pipe, see Fig. 5. As described previously buildup of sand in the blinded section together with the stagnant zone there diminishes particle impacts and therefore erosion.

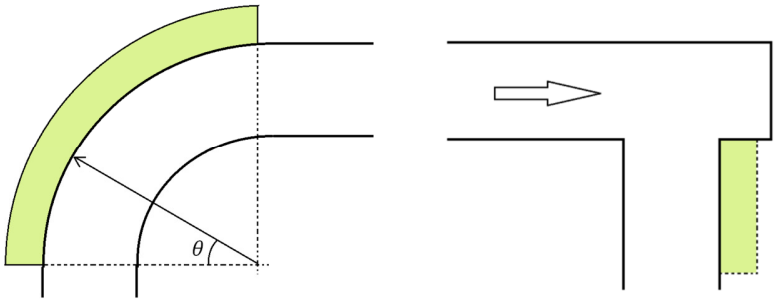

Fig. 5: Principal picture depicting zones of maximum erosion were erosion rates were sampled during simulations.

The simulations presented below are compared to some of the main correlations for sand erosion prediction in use by the industry, the correlations presented by Det Norske Veritas (DNV) report DNV RP O501 from the work of Kvernvold and the alternative to API RP 14E proposed by Salama. Furthermore comparisons and comments are made with correlations proposed by Venkatesh et al. and Arnold et al. Details about the correlations are given in section 2.1.

Simulations over the size range for 1 m/s are presented in Fig. 6 and 7. Simulations for 10 m/s and 50 m/s are given in Appendix 3. As can be seen from the graphs the size dependent trend is preserved under changing flow velocity. It is expected that small particles will be highly affected by drag and therefore display a low erosion rate. As the particle becomes larger erosion should increase until inertia dominates over drag and thereafter no size effect would be expected. Contrary to this it can be seen that maximum erosion is obtained at intermittent particle sizes with a subsequent lowering of wear rates thereafter.

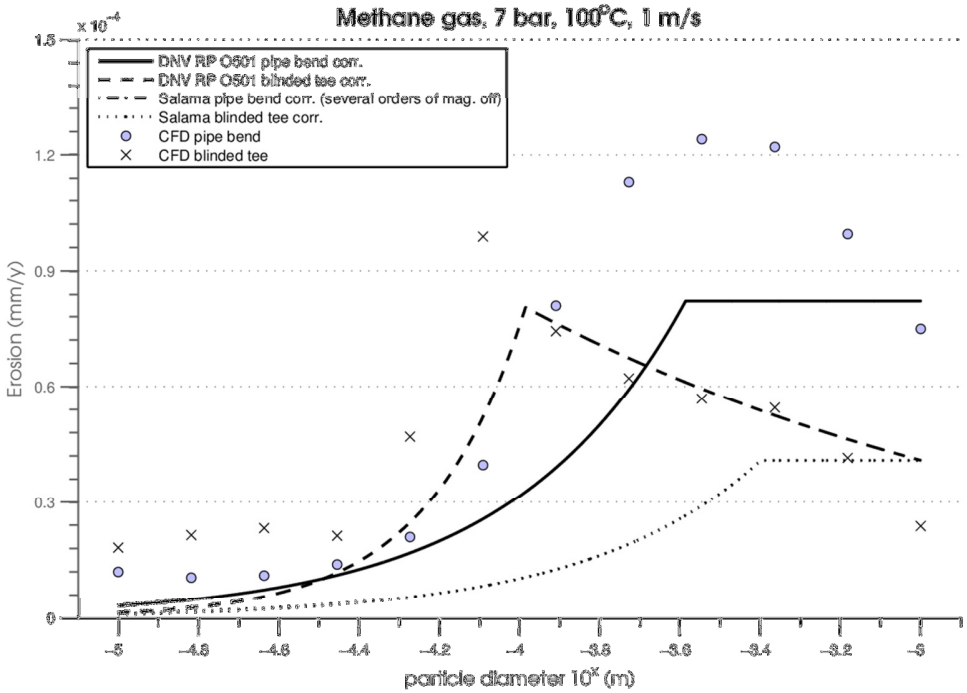

Fig. 6: Rate of maximum erosion for pipe bend and blinded tee at a flow velocity of 1 m/s. Data as markers are compared to correlations depicted by dashed and solid lines. Note that the Salama pipe bend correlation predicts erosion rate up to two orders of magnitude larger than indicated by simulations.

The size range most prevalent for sand is depicted in Fig. 7.

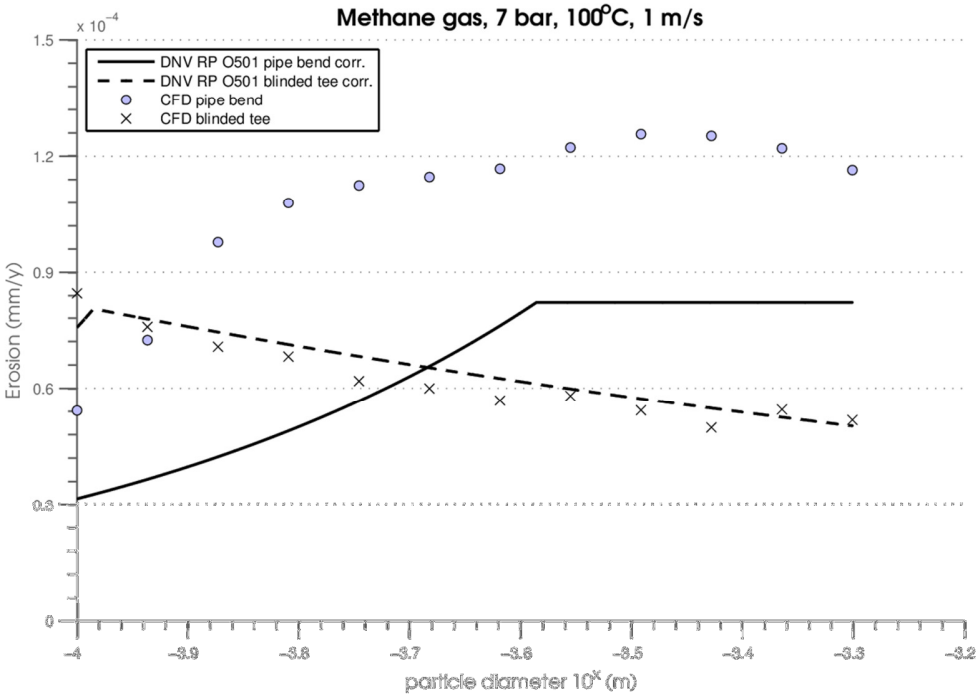

Fig. 7: Rate of maximum erosion in the size range of most sands.

The DNV RP 0501 correlation is by far the most sophisticated correlation under investigation while it both includes particle size effects as well as geometry and sizing factors such as pipe diameter and radius of curvature for the pipe bend. The Salama correlation also includes particle size effects as can be seen from the plateau of wear rates after a certain threshold particle size for the pipe bend. The DNV correlation for the blinded tee predicts an erosion maximum as indicated by the CFD results. The maximum arises while at higher Stokes numbers the particles doesn't deviate from their trajectory and collides with the blinded tee section resulting in fewer impacts in the outlet section therefore reducing rate of erosion, Fig. 8. As can be seen from the graphs there is good agreement between the DNV correlation and CFD simulations for the blinded tee.

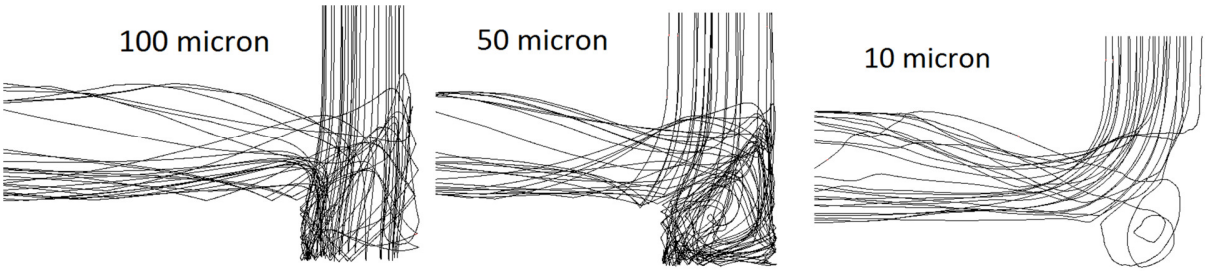

Fig. 8: Representative particle trajectories depicting the transition from mainly collisions with the blind to outlet collisions only.

The behavior associated with the maximum for the pipe bend mentioned above will now be addressed in some detail. The phenomenon is somewhat more complex and stems from a combination of the drag force, angle dependent function of erosion and the restitution coefficient. For large stokes numbers the particles hit the pipe bend wall without any drag induced trajectory deviation. After the first impact most particles leave the pipe bend section without any further impacts at a radius of curvature of 1.5 pipe diameters. Only a fraction of incoming particles, as schematically depicted in Fig. 9, impact the bend section more than once. Seen from the inlet section even a smaller fraction impact twice etc.

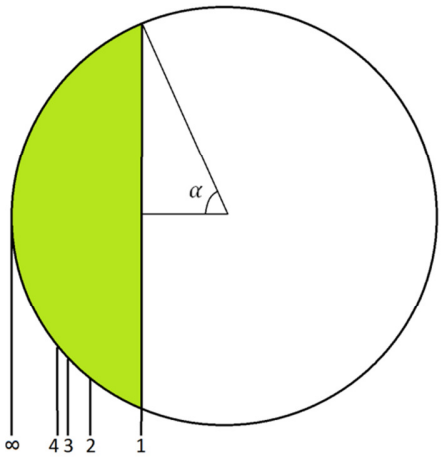

Fig 9: Fraction of incoming particles, impacting more than once schematically highlighted by the

colored field. The circle represents the pipe seen from the inlet section of the bend spanning to the right. Also note that the highlighted zone is conceptual. In reality, particles approaching the bend in top and bottom also undergo multiple impacts.

It can be shown mathematically that only a slight decrease in impact angle associated with a small drag effect upon particles dramatically increases the fraction of incoming particles impacting more than once, therefore augmenting the rate of erosion for smaller sand particles. As particles become smaller and the drag starts to dominate a large fraction of trajectories will not lead to impact, reducing the rate of erosion, see Fig. 10.

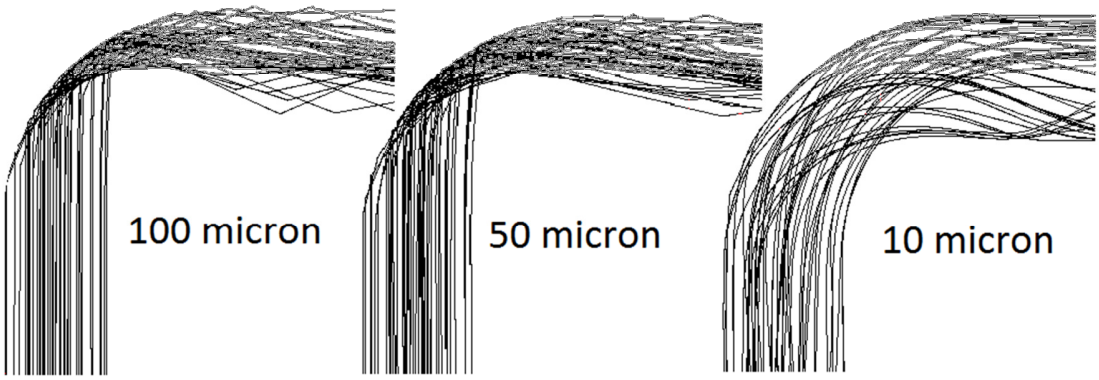

Fig. 10: Representative particle trajectories for the pipe bend.

Erosion patterns at the symmetry plane of the pipe bend as highlighted in Fig. 5 are given in Fig. 11. The behavior described above can clearly be noted as a dramatic increase in erosion when particles become smaller and a subsequent lowering of rates when drag starts to dominate.

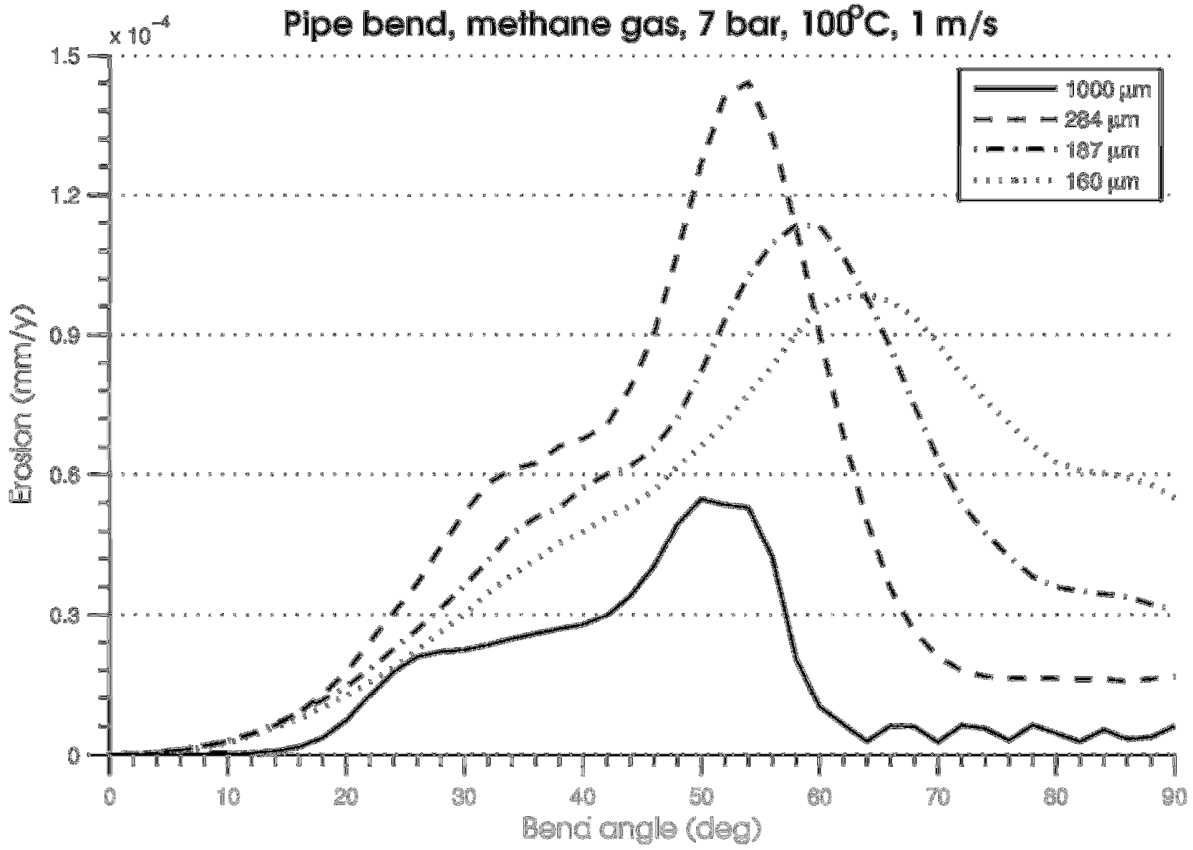

Fig. 11: Erosion increases between 1000 µm particles and 284 µm due to the dramatic increase in multiple impact events with a subsequent lowering of rates after 284 µm due to less particle impacts caused by increased drag. At a bend angle of more than 50° the outer wall is obscured due to curvature for incoming particles.

Furthermore the overall wear pattern is controlled by the impact angle function maximizing erosion at impact close to 30°. Secondary and tertiary collisions are almost exclusively associated with small impact angles and lower velocity magnitudes due to the restitution coefficient. A lower velocity magnitude is severely punished by the 2.6 velocity exponent in the wear equation greatly diminishing wear contribution for slow moving particles.

4.2.3 Particle shape

Sand particles are irregular and deviate more or less from spherical particles. Their impacts are also non ideal and dependent upon impact angle. Particle trajectories are therefore affected via the change in drag force and irregular impact events. To account for this it might be necessary to use a non-spherical drag law such as the Haider-Levenspiel drag law and the non-constant restitution coefficients. Simulations were carried out with the polynomial expansion restitution coefficients proposed by Froder et al. for sand impingement on AISI 4130 steel. In Fig. 12 the Forder restitution coefficients are compared to the stochastic restitution coefficients of

Sommerfeld and Tabakoff derived from experiments on sand impact on aluminum surfaces. Their restitution coefficients are sampled from a stochastic distribution with a mean and standard deviation given by polynomials similar to those of Froder et al.

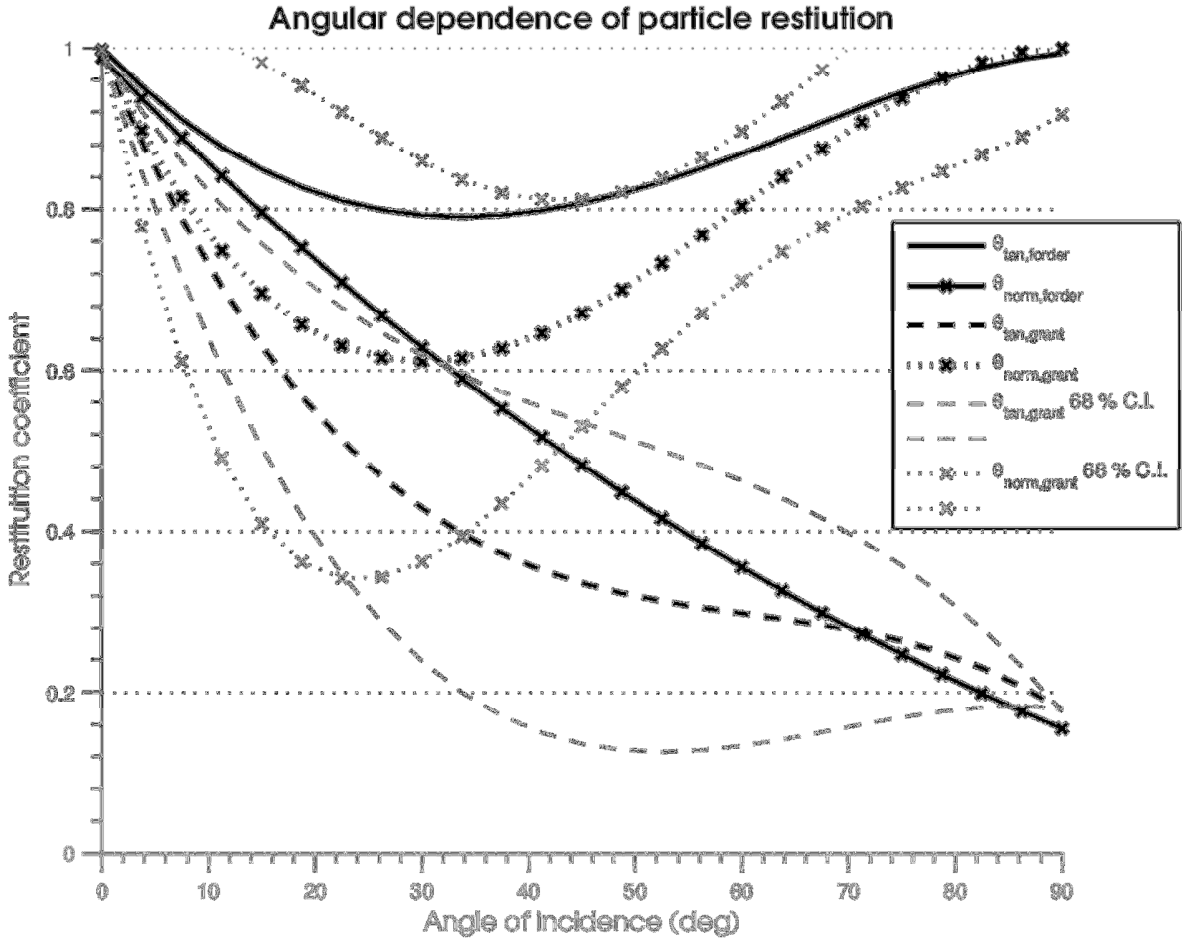

Fig. 12: Comparison of restitution coefficient polynomials used for predicting sand impact characteristics.

The Froder restitution coefficients were compared to the standard constant restitution coefficients often used when modeling sand erosion and other particle laden flows. In Fig. 13 it can be seen that using a constant restitution coefficient of 0.9 affects the predicted wear rates, resulting in offsets of about 5 - 10 %.

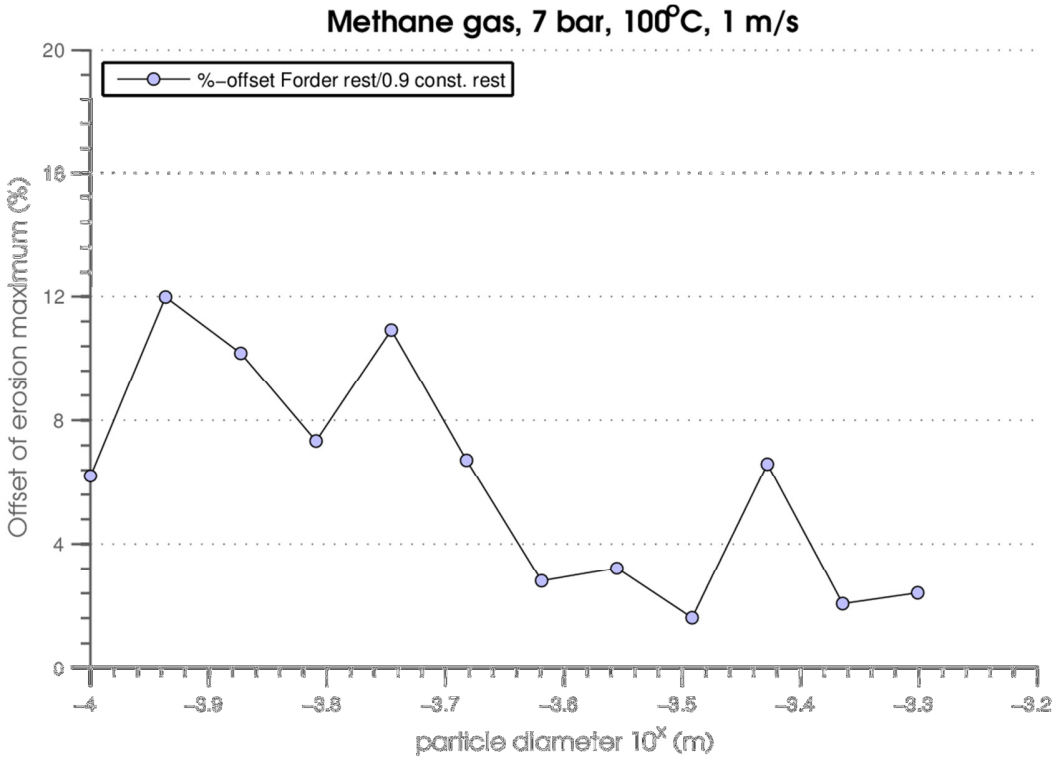

Fig. 13: Change in maximum erosion rate using Froder restitution coefficients compared to 0.9 constant restitution coefficients.

4.2.4 Flow velocity

The effect of changing flow field velocities was investigated over a velocity range of 1 m/s to 50 m/s. Furthermore a comparison between a number of correlative wear predictive methods and their ability to handle changes in flow field velocity were conducted for 500 micron particles. The results from simulations are presented in figure 14.

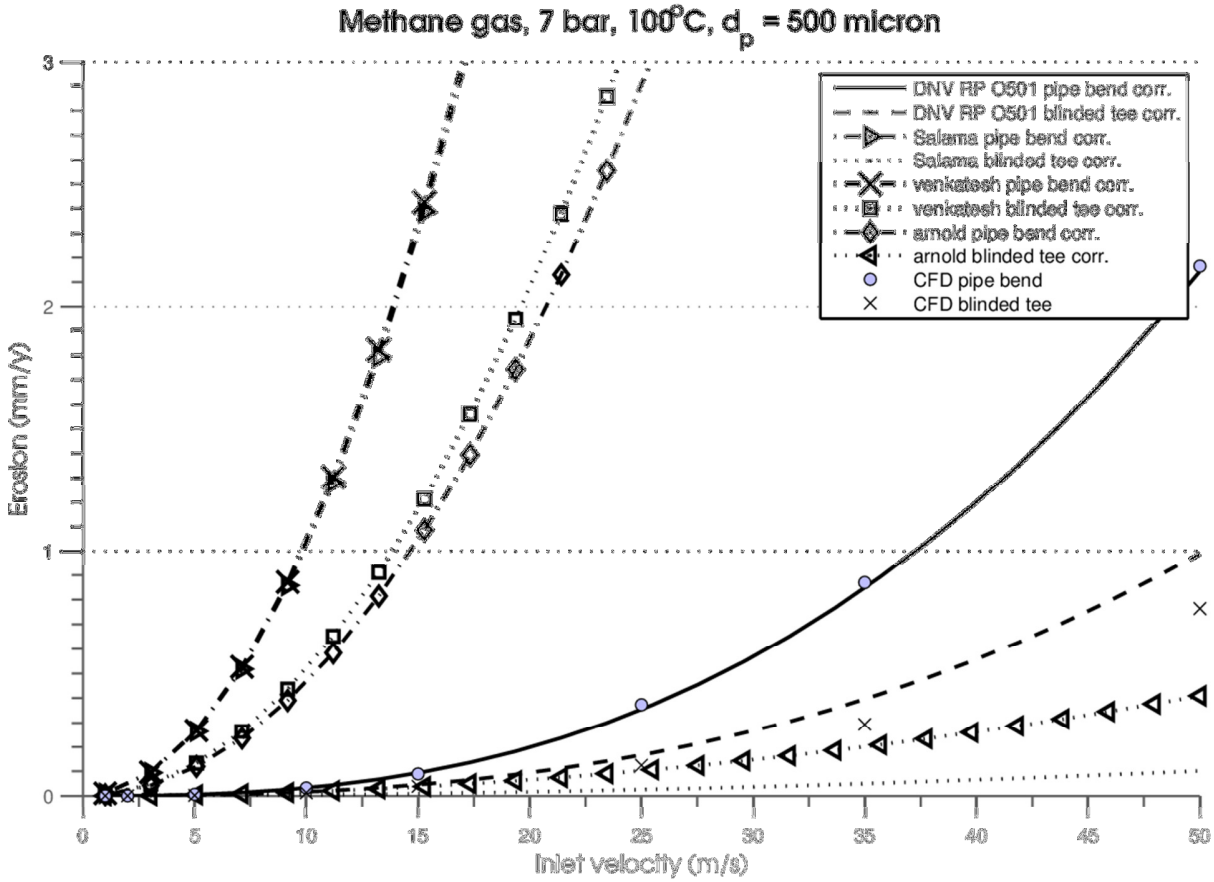

Figure 14: Erosion rate dependence upon floe velocity as compared to correlative methods.

As seen in the figure the DNV correlation is the one that describes the erosion for both the blinded tee and pipe bend best. Especially the pipe bend correlation has a good agreement with simulations. Most of the correlations are conservative predicting erosion rates several orders of magnitude above the rates indicated by simulations, except the Salama blinded tee correlation. This type of analysis is often used in industry and aims at inferring whether or not production rates can be increased without sustaining excessive erosive wear damage. This kind of analysis is often carried out with any of the correlations depicted in Fig. 14 above, often resulting in extremely conservative results, limiting flow field velocities well below what would be tolerated. Salama compared the correlations proposed by university of Tulsa and the DNV RP O501 correlations which both are stated to be based on experimental measurements and subsequent extrapolation outside the experimentally determined interval and found, in certain cases, disparities in predicted erosion rate of several order of magnitudes.

4.2.5 Geometry

CFD-simulations were compared with some correlations ability to handle changes in pipe. The production rate was set constant, varying the pipe diameter. The curvature for the pipe was kept constant. The production used was given by the case having a gas velocity of 10 m/s and a pipe diameter of 100 mm. A velocity of 62.5 m/s was needed to reach the same production for the 40 mm pipe diameter case. The results are presented in Fig. 15.

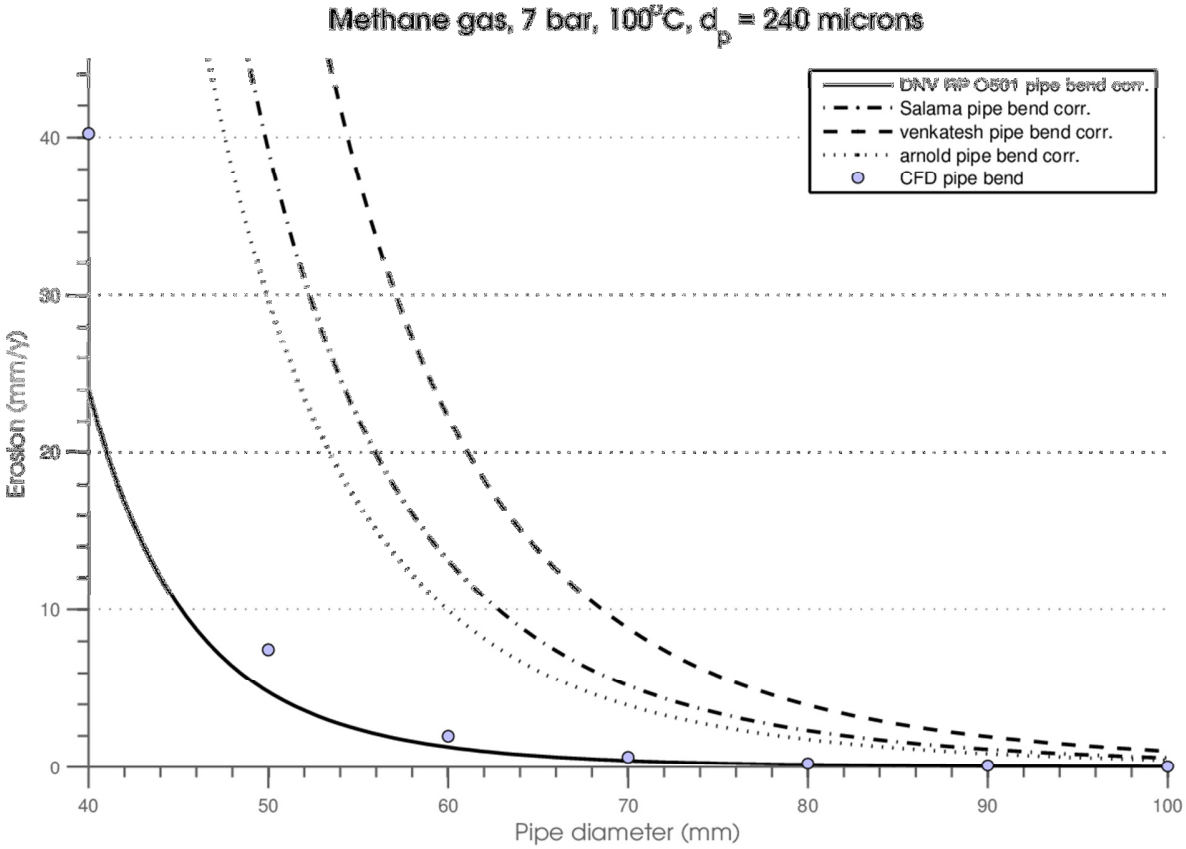

Figure 15: Pipe diameter dependency of Eulerian model as compared to the DNV correlation

Figure B highlights the dramatic impact of changing pipe diameter to counter erosive wear damage. Another thing to notice is that all correlations except the DNV RP are highly conservative when it comes to estimation of erosion compared to our simulations. Pipe wall thickness in the oil/gas industry are usually between 0.4 and 70 mm which means that a large part of the pipe will erode if one of the smaller diameters are used within one year of production.

4.2.6 Experimental validation

Replication of the experimental set published by Wong is presented in this section. The set was used in order to validate the Lagrangian model against actual measurements. Letting particles collide with the alumina plate led to erosion patterns as shown in figure 16.

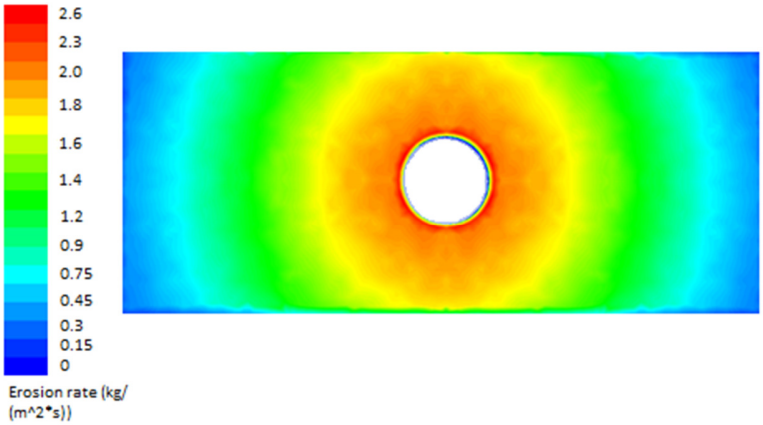

Figure 16: Erosion patterns

The measured erosion is compared to simulations in Fig. 17. The data is marked with markers and simulated wear rates with correspondingly marked lines.

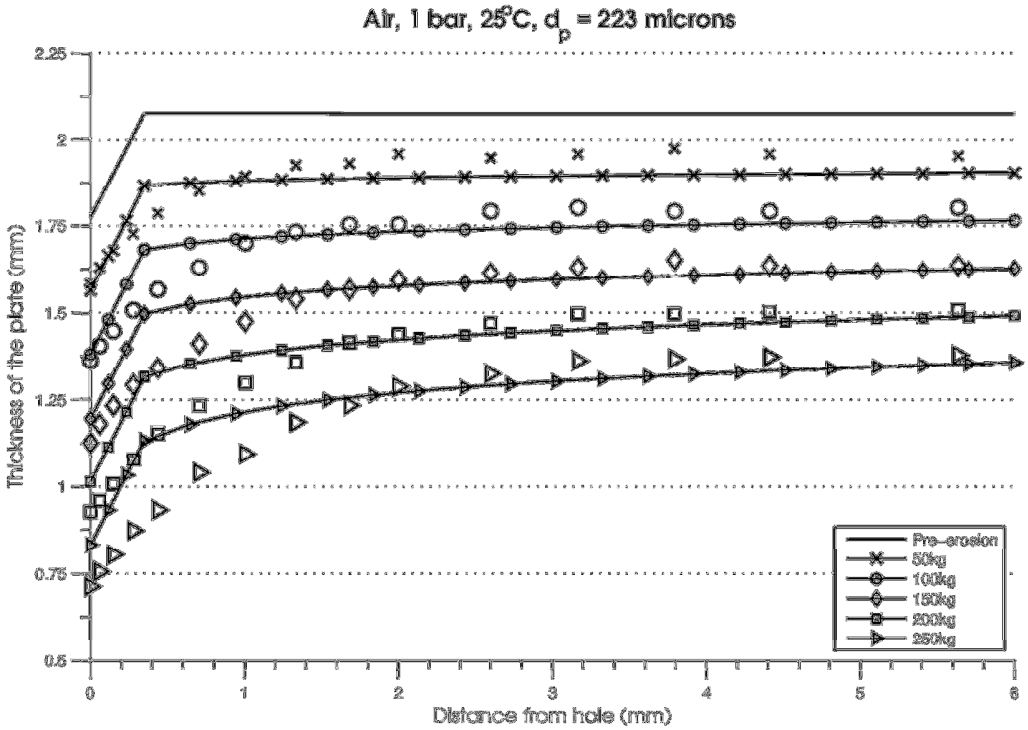

Figure 17: Erosion results for the experimental set. Dotted lines are CFD-simulations and corresponding free dots to each line represents experimental measurements.

Close to the center, the greatest difference between experimental data and simulations can be observed. This difference is increasing as the wear process progresses. The wear process here differs while impacting particles might dent the edge and rip of material while mechanically deforming the edge. This phenomenon was confirmed by microscope investigation of the surface as reported by Wong.

4.3 Eulerian-Eulerian

The following section begins with a demonstration of the difficulties associated with the adaptation of Lyckowskis erosive wear model to larger non integer velocity exponents and proposes a simple workaround. However the severity of the assumption made might possibly compromise the benefit with more accurate velocity dependence. The section is concluded with some simulations indicating the applicability of the wear model.

4.3.1 Adaptation of the Lyckowski model

Recent experimental investigations of sand erosion on steel grades such as DNV RP O501 suggests a velocity dependence stronger than that of Finnie's original wear model. Lyczkowski derived their model for granular flows using Finnie's model as a basis and therefore a velocity exponent of two. In order to obtain accurate results of wear on steel grades the derivation has to be redone with a higher velocity exponent of 2.6, or else a change in velocity from e.g. 1 m/s to 50 m/s will yield an error of more than one order of magnitude. However doing this adaptation has proven to be more difficult than what was first be expected. This section highlights the problem and proposes a simple solution under some assumptions.

Finnie's model, Eq. (X), as stated by Lyczkowski gives the volume removed by one particle impact, where c_w is the instantaneous particle speed, α the angle of attack and m the particle mass, Eq. (55).

$$W = B_F m c_w^2 f(\alpha) \tag{55}$$

Where

$$B_F = \frac{C_F}{P_H \psi H} \tag{56}$$

And

$$f(\alpha) = \begin{cases} \sin 2\alpha - 3\sin^2 \alpha, & \alpha \leq 18.43° \\ 1/3 \cos^2 \alpha, & \alpha > 18.43° \end{cases} \tag{57}$$

From the single particle equation (55) one can obtain the erosive wear for the whole velocity range via integration with the maxwellian distribution, see Eq. (58).

$$E_{tot} = \int_{\vec{c}_w \cdot \vec{n} > 0} (\vec{c}_w \cdot \vec{n})\, B_F m c_w^2 f(\alpha) f_w(\vec{r}, C_w, t) d\vec{c}_w \tag{58}$$

The integration is carried out setting the fluctuating velocity $\vec{C}_w$ equal to the difference of the instantaneous and mean velocities, $\vec{c}_w - \vec{v}_w$. Furthermore one uses the relation $c_w^2 \simeq C_w^2 + v_w^2 + 2C_w v_w \sin\theta$, and that $\vec{c}_w \cdot \vec{n} = \vec{C}_w \cdot \vec{n} + \vec{v}_w \cdot \vec{n} = C_w \cos\theta$ where $\theta = \pi/2 - \alpha$.

$$E_{tot} = mB_F \frac{n}{(2\pi T)^{\frac{3}{2}}} \int_{\vec{c}_w \cdot \vec{n} > 0} C_w \cos\theta \, (C_w^2 + v_w^2 + 2C_w v_w \sin\theta) \, f(\pi/2 - \theta) \exp\left(-\frac{C_w^2}{2T}\right) d\vec{c}_w$$

$$= \left[d\vec{c}_w = d\vec{C}_w = C_w^2 \sin\theta \, dC_w d\theta d\phi\right]$$

$$= mB_F \frac{n}{(2\pi T)^{\frac{3}{2}}} \iiint_{C_w=0 \; \theta=0 \; \phi=0}^{\infty \; \pi/2 \; 2\pi} (C_w^5 + C_w^3 v_w^2 + 2C_w^4 v_w \sin\theta) f(\pi/2$$

$$- \theta) \exp\left(-\frac{C_w^2}{2T}\right) \sin\theta \cos\theta \, dC_w d\theta d\phi$$

This integral is readily evaluated noting the result of expression (59).

$$\int_0^\infty x^n e^{-ax^2} dx = \begin{cases} \frac{1}{2}\Gamma\left(\frac{n+1}{2}\right) \Big/ a^{\frac{n+1}{2}} & , n > -1, a > 0 \\ \frac{(2k-1)!!}{2^{k+1} a^k} \sqrt{\frac{\pi}{a}} & , n = 2k, k \text{ integer}, a > 0 \\ \frac{k!}{2a^{k+1}} & , n = 2k, k \text{ integer}, a > 0 \end{cases} \quad (59)$$

As can be seen it is possible to carry out this derivation while one can exploit the trigonometric relation between the instantaneous, fluctuating and mean field velocities. This is however not possible for other velocity exponents than even integers. One way of tackling this problem might be a series expansion in even integers, found by a least square method around a desired operating point. For our simulations we used a simplification that captures the velocity dependency to some degree. The instantaneous velocity is a function of the mean and fluctuating velocity as well as the angle between them, $c_w = g(C_w, v_w, \theta)$. By partially neglecting this functional dependency, the integral can still be evaluated, $c_w^{2.6} = c_w^2 c_w^{0.6} = c_w^2 v_w^{0.6}$. By doing so and also replacing Finnie's expression B_F with the coefficient proposed by DNV RP O501, dividing by the material density of the impacted surface and multiplying by the unit conversion factor, $C_{unit} = 3.15e^{10}[^S/_{year}]$ one obtains our proposed modification to Lyczkowski's wear formula, Eq. (60).

$$E_{tot} = \frac{2\alpha_s \alpha_s K C_{unit}}{\rho_s} \left[\frac{v_w^{0.6}(2T)^{3/2}}{10\sqrt{\pi}} + \frac{v_w^{2.6}}{20}\sqrt{\frac{2T}{\pi}} + \frac{9}{100} v_w^{1.6} T\right] \quad (60)$$

4.3.3 Effect of changing velocity

It should first be pointed out that the Eulerian simulations don't reproduce the same magnitude of erosion as indicated by the Lagrangian simulations; the discrepancy is of approximately one order of magnitude. However the DNV correlation indicates wear results in the close vicinity but as demonstrated in section X these results might be flawed. The effect of changing velocity is given in Fig. 18. It can be seen that the trend, as indicated by the DNV correlation and the Eulerian model, is similar but not identical. The relative change in magnitude decreases as velocity increases, indicating a somewhat too strong velocity dependency.

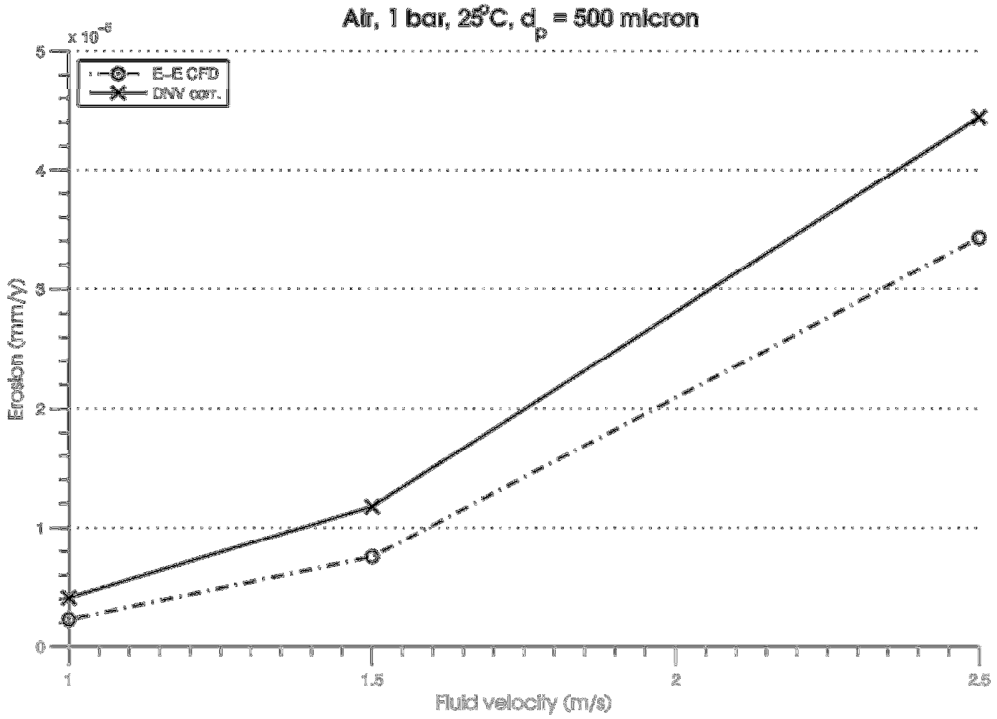

Fig. 18: Velocity dependence of Eulerian model as compared to the DNV pipe bend correlation.

4.3.3 Effect of particle diameter

As depicted in Fig. X, the diameter dependence of the Eulerian model indicates a positive trend resulting in larger wear rates as particles become larger. The DNV correlation however predicts that the particle size effect should be insignificant in this size region resulting in constant wear rates as particles become larger from 250 µm. To the contrary, the Lagrangian simulations indicate a weak negative tendency as particles become larger as can be noted in Fig. 19.

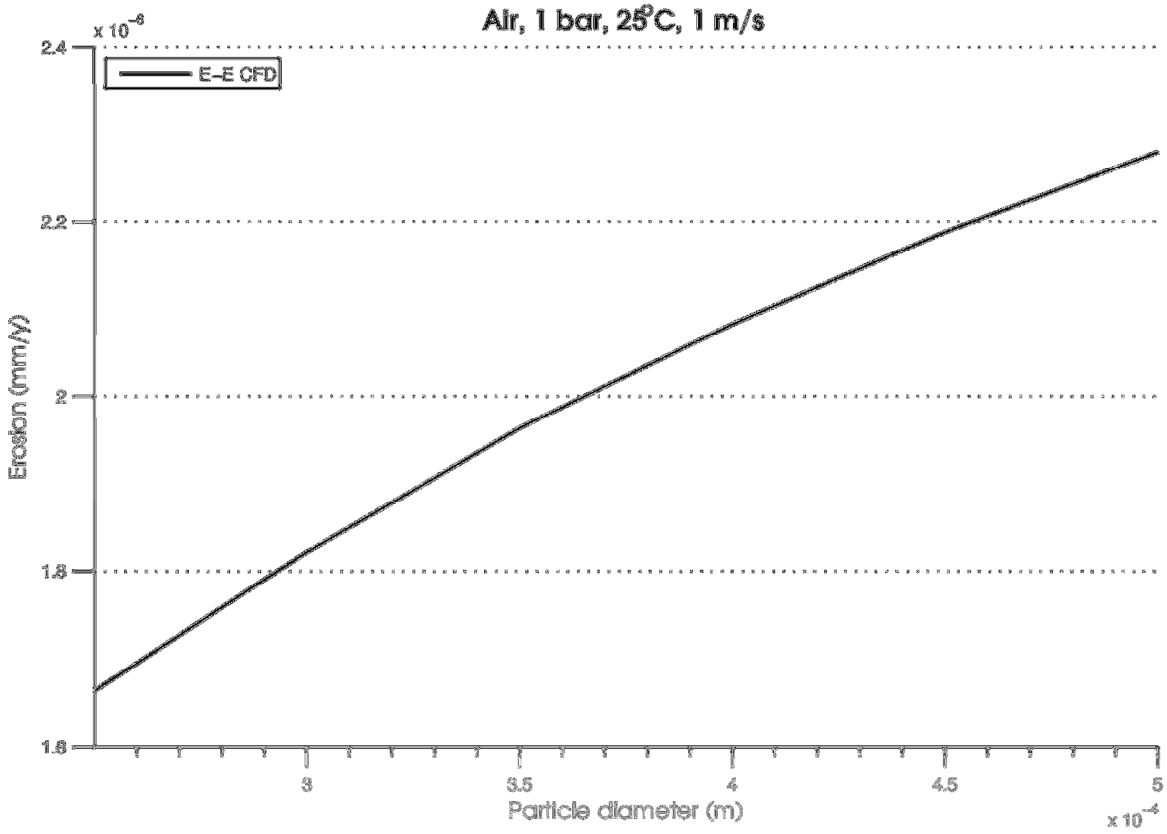

Fig. 19: Particle diameter dependency of the Eulerian model in the size range 250 µm to 500 µm.

4.3.4 Eulerian erosion pattern

The ability of a wear model to predict the spatial distribution of wear is of uttermost importance while such predictions might be used as a foundation for new design features or reinforcing measures taken to avoid pipe breakage such as protective films. Fig. 20 compares the erosion pattern produced by our Lagrangian and Eulerian models. Note that the curves have been normalized due to the large difference in wear magnitudes. As can be concluded from the figure, the Eulerian model reproduces a similar overall shape of the wear pattern. The pattern is however slightly translated towards the outlet sections and doesn't reproduce the same tail as the Lagrangian curve.

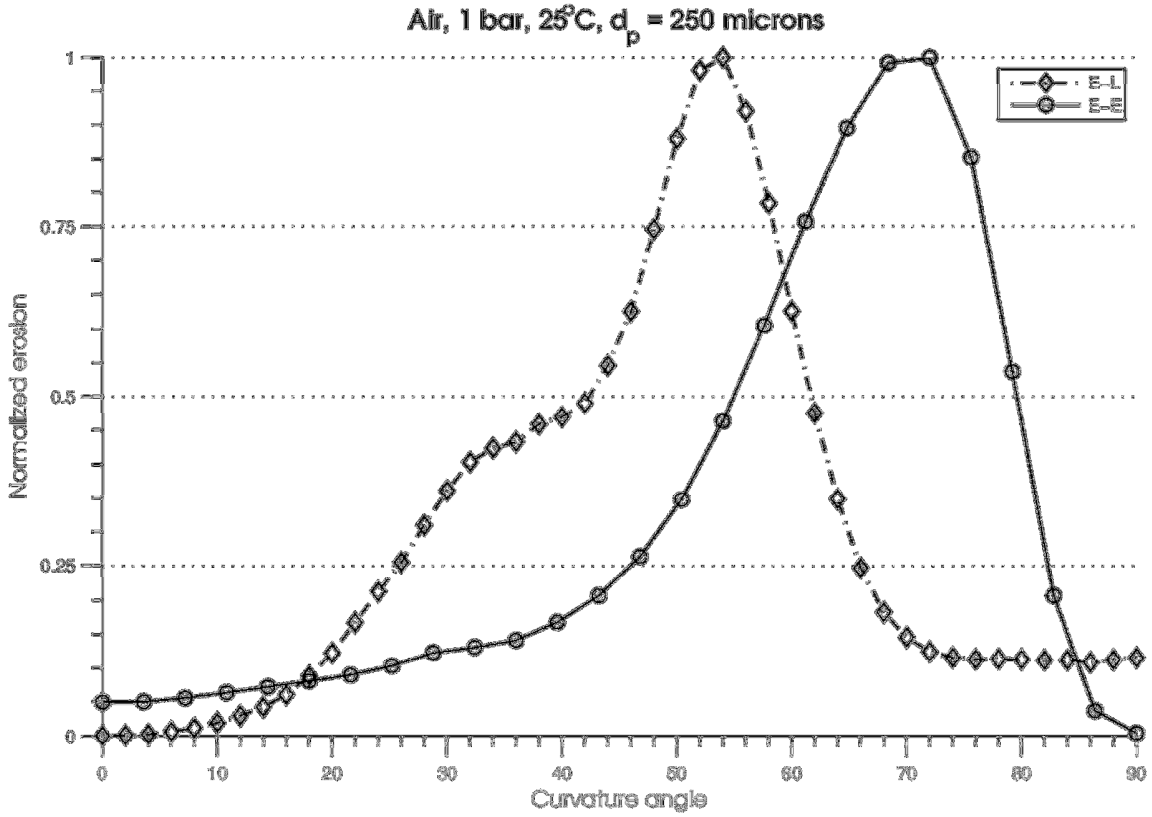

Fig. 20: Erosive wear pattern of Eulerian model compared to Lagrangian. Note that the curves have been normalized due to rate differences of more than one order of magnitude.

4.4 DNV RP O501 pipe bend correlation for low density fluids

Our Lagrangian simulations for erosion in pipe bends with air and methane resulted in closely resembling wear rates. This is expected while air and methane under standard conditions have similar densities and viscosities. The DNV RP O501 correlation was in agreement with most of our results. However at lower flow velocities, approximately below 10 m/s the DNV correlation suddenly predicted much lower wear rates in air than in methane, in direct contrast to what one would expect. Our results indicate that the pipe bend correlation undergoes a step change in correction coefficients at fluid densities just above that of NTP air. The step change results in more than one order of magnitude smaller wear rates just after the step change. Fig. 21 depicts the step change for various flow velocities into a pipe bend with a radius of curvature of 1.5D.

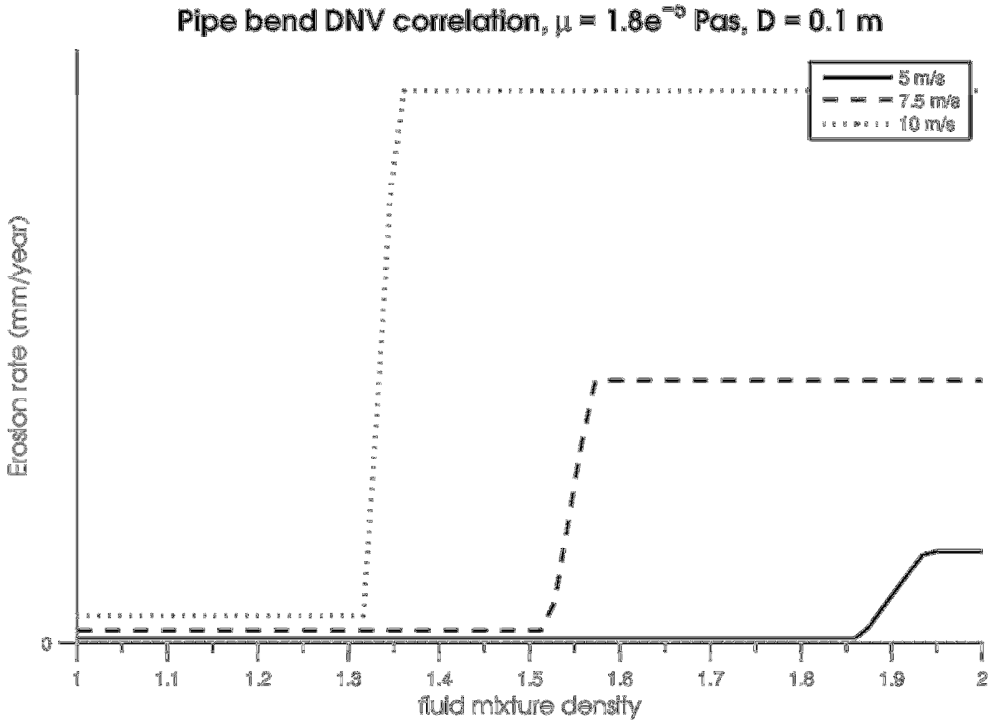

Fig. 21: Predicted erosion rate versus fluid mixture density by DNV RP O501 pipe bend correlation.

This result is clearly obscure. Our simulated erosion rates in methane at conditions where this occurs agree with the correlation and are of the same magnitude as for air. Therefore we believe that one risks to dramatically unde-restimate erosion rates for low density media at lower flow velocities using the pipe bend correlation alone. The step change in the correlation is the result of a parameter, γ_c, become negative.

5. Conclusions

Lagrangian simulations were conducted investigating erosion in pipe bends and blinded tees. Parameter variations were carried out spanning over particle size, flow field velocity, type of fluid, geometry dimensions, choice of restitution coefficients and other simulation parameters such as discretization scheme, mesh refinement, particle sampling volume and choice of turbulence model. It was found that choice of restitution coefficients have a significant impact upon erosion rates. Many sand erosion studies have employed constant coefficients which might lead to offsets in wear magnitude as well migration of the wear pattern. Our results using Froder et als restitution model suggest that experimentally derived polynomial restitution coefficients dependent upon the impact angle, which are specific to the nature of the impacted material, might lead to a significant improvement in wear predictions in the Lagrangian framework.

Contrary to wear predictive correlations such as DNV RP O501 or the model proposed by Salama and Venkatesh our findings suggests that the effect of particle size upon erosion in pipe bends might be more elaborate. We found an erosion maximum to be present at intermediate particle sizes around 250 μm for all velocities. Correlative methods predict that after a certain threshold, erosion rates should be size independent. We suggest that this behavior stems from events occurring at particle sizes where drag forces begins to affect particle trajectories. Particles mainly affected by inertia, travelling in straight lines, tend to lead to few impact events while smaller particles whose trajectories have deviated, impacts with smaller impingement angles, leading to more consecutive impacts. At even smaller particle diameters the amount of particles impacting are markedly decreased as drag dominates over inertia. Therefore a point of maximum erosion rate is formed for intermediate sand particles.

A similar maximum is seen for intermediate particle sizes in the blinded tee. This behavior however is in line with correlations such as DNV. This behavior is also more straightforward to explain. Small particles follows the streamlines and few impacts occurs in the outlet section, as particles become larger more impacts occur until particles deviate completely and hit the blinded section of the tee.

Our CFD-simulations also suggests that the DNV correlation for the pipe bend breaks down at lower velocities, < 10 m/s, for low density media such as air. Predicted erosion rates suddenly drop more than one order of magnitude, predicted by the DNV correlation, at a certain threshold. The threshold is reached when the dimensionless critical particle diameter, γ_c, suddenly becomes negative resulting in a step change in the correction parameters. This trend in erosion rates are not in line with our simulations which indicates a slight lowering of erosion rates as the fluid properties such as density and viscosity approaches a denser gas such as methane from that of air. Therefore we suggest cautious use of the DNV correlation and complementary use of CFD at low flow velocities for low density mixtures or one might risk serious implications.

Furthermore an Eulerian model originally developed for use in packed beds has been used for simulation of pipe components. This approach has to our knowledge never been used for such a

system and our results might give insights into the incentives for such a model. The model, originally derived by Lyckowski, needs to be adapted to higher velocity exponents to conform to Lagrangian models for steel components. We adapted the model with a higher velocity exponent by neglecting part of the fluctuating velocity contribution to erosion.

Our results suggest that the proposed variable grouping can reproduce the trend in velocity and particle diameter as expected. Furthermore erosion patterns similar to those of Lagrangian simulations were reproduced for the pipe bend. It should be noted that the proposed approached was associated with severe convergence issues as well as mesh independence problems.

The main incentive for the Eulerian model is the ability to model lower erosion efficiencies in dense mixtures; however our simulations fail to yield reasonable wear magnitudes accurate enough to model such effects. In the light of our Lagrangian simulations however one can argue that such effects won't be discernible except in geometries with extreme differences in loadings such as sand traps or the blinded section of a tee; while many other elements of the modeling procedure such as restitution, drag and erosive wear models induce uncertainties of greater magnitude. Also many phenomena such as the topology change that occurs, while the erosive wear advances, which changes flow conditions and therefore wear rates takes precedence over the drop in efficiency at higher loadings. When deriving such a model in the Eulerian framework much resolution crucial for accurate wear prediction is lost, such as the ability to determine impingement angles. Therefore even if one were to resolve the difficulties associated with the procedure, we deem the outlook for accurate efficiency estimations in denser regions using an Eulerian approach to be grim.

Due to the high complexity of the wear process, correlative methods are only likely to work for narrow ranges of very specialized geometries or to be extremely conservative as shown by comparison. Therefore Lagrangian simulations which can be conducted with relative ease have potential to result in large economical savings in dimensioning against erosion. Future efforts with the Eulerian model might focus on adapting the proportionality constant to experimental data and optimizing the choice of momentum coupling between primary and secondary phases to obtain a more accurate size dependence. In the overall erosion modeling field we suggest that more physics should be included in simulations primarily focusing upon modeling of topology changes. The first studies with consecutive re-meshing as a tool for mimicking topology changes have yielded very promising results.

References

1. Finnie, *Erosion of surfaces by solid particles.* Wear, 1960. 3(2): p. 87-103.
2. Bitter, *A study of erosion phenomena part I.* Wear, 1963. 6(1): p. 5-21.
3. Bitter, *A study of erosion phenomena: Part II.* Wear, 1963. 6(3): p. 169-190.
4. Humphrey, J.A.C., *Fundamentals of fluid motion in erosion by solid particle impact.* International Journal of Heat and Fluid Flow, 1990. 11(3): p. 170-195.
5. Laitone, J.A., *Aerodynamic effects in the erosion process.* Wear, 1979. 56(1): p. 239-246.
6. Gnanavelu, A., et al., *An integrated methodology for predicting material wear rates due to erosion.* Wear, 2009. 267(11): p. 1935-1944.
7. Wong, C.Y., et al., *Predicting the material loss around a hole due to sand erosion.* Wear, 2011(0).
8. McLaury, B.S., et al., *Distribution of Sand Particles in Horizontal and Vertical Annular Multiphase Flow in Pipes and the Effects on Sand Erosion.* Journal of Energy Resources Technology, 2011. 133(2): p. 023001-10.
9. Lester, D.R., L.A. Graham, and J. Wu, *High precision suspension erosion modeling.* Wear, 2010. 269(5–6): p. 449-457.
10. Lyczkowski, R.W. and J.X. Bouillard, *State-of-the-art review of erosion modeling in fluid/solids systems.* Progress in Energy and Combustion Science, 2002. 28(6): p. 543-602.
11. Gustavsson, M. and A.E. Almstedt, *Two-fluid modelling of cooling-tube erosion in a fluidized bed.* Chemical Engineering Science, 2000. 55(4): p. 867-879.
12. Achim, D., et al., *Tube erosion modelling in a fluidised bed.* Applied Mathematical Modelling, 2002. 26(2): p. 191-201.
13. He, Y., et al., *Prediction on immersed tubes erosion using two-fluid model in a bubbling fluidized bed.* Chemical Engineering Science, 2009. 64(13): p. 3072-3082.
14. Lyczkowski, R.W. and J.X. Bouillard, *Erosion Calculations in a Two-Dimensional Fluidized Bed.* Proceedings of the Ninth International Conference on Fluidized Bed Combustion, 1987. 2: p. 697 - 706.
15. Ushimaru, K., *Design and Applications of the Novel Slurry Jet Pump.* Energy International, 1984(E184-108).
16. Ding, J. and R.W. Lyczkowski, *Three-dimensional kinetic theory modeling of hydrodynamics and erosion in fluidized beds.* Powder Technology, 1992. 73(2): p. 127-138.
17. DetNorskeVeritas, *Recommended practice RP O501 Erosive wear in piping systems.* 2007(4.2).
18. Salama, M.M., *An Alternative to API 14E Erosional Velocity Limits for Sand-Laden Fluids.* Journal of Energy Resources Technology, 2000. 122(2): p. 71-77.

Appendix 1 Partial slip boundary UDF

The following C++ script enables implementation of the partial slip boundary condition described under section 2.3.1.6 into ANSYS Fluent 14.0 as a user defined function (UDF). Fluent works with a global coordinate system and velocity vectors can only be called upon in the global basis, therefore a coordinate transformation matrix has to be calculated at every face such that the velocity vectors can be transformed to a local basis at each face. Thereafter the calculations described in section 2.3.4 can be carried out and the resulting shear components are transformed back to the global basis. The code is adapted to both parallel and serial usage.

```
#include "udf.h"
#include "mem.h"
#include "surf.h"
#include "metric.h"
DEFINE_PROFILE(wall_xshear, sandthread, index)
{
	int zone_ID;
	real nx, ny, nz;
	real a11, a12, a13, a21, a22, a23, a31, a32, a33;
	real b11, b12, b13, b21, b22, b23, b31, b32, b33, determ, root1;
	real nvel, tvel1, tvel2, nshear, tshear1, tshear2, shearx, sheary, shearz, ginner, granvisk2, limit3=1, limit2=3, limit1=1, lim=0.01;
	real granvisk, lambdap;
	real diam=0.00005, rhos=2600, rescof=0.9, gzero;
	real NV_VEC(velvec), NV_VEC(A);
	face_t faceidentifier;
	cell_t closecellidentifier;
	Thread *cell_thread;
	begin_f_loop(faceidentifier,sandthread)
	if PRINCIPAL_FACE_P(faceidentifier,sandthread)
	{
		#if !RP_HOST
		zone_ID=THREAD_ID(sandthread);
		F_AREA(A,faceidentifier,sandthread);
		A[0]=-1*A[0]/NV_MAG(A);
		A[1]=-1*A[1]/NV_MAG(A);
		A[2]=-1*A[2]/NV_MAG(A);
		closecellidentifier=F_C0(faceidentifier,sandthread);
		cell_thread=THREAD_T0(sandthread);
		NV_D(velvec,=,F_U(faceidentifier,sandthread),F_V(faceidentifier,sandthread),F_W(faceidentifier,sandthread));
		nx=A[0];
		ny=A[1];
		nz=A[2];
		root1=sqrt(pow(ny,2)+pow(nz,2));
		a11=nx; /* Orthonormal basiS */
		a12=0;
		a13=root1;
		a21=ny;
		a22=nz/root1;
		a23=-nx*ny/root1;
		a31=nz;
		a32=-ny/root1;
		a33=-nx*nz/root1;
		determ=a11*(a33*a22-a32*a23)-a21*(a33*a12-a32*a13)+a31*(a23*a12-a22*a13);
		b11=(a33*a22-a32*a23)/determ; /* Inverse transformation matrix for back transformation */
		b12=-1*(a33*a12-a32*a13)/determ;
		b13=(a23*a12-a22*a13)/determ;
		b21=-1*(a33*a21-a31*a23)/determ;
		b22=(a33*a11-a31*a13)/determ;
		b23=-1*(a23*a11-a21*a13)/determ;
		b31=(a32*a21-a31*a22)/determ;
		b32=-1*(a32*a11-a31*a12)/determ;
		b33=(a22*a11-a21*a12)/determ;
		nvel=b11*velvec[0]+b12*velvec[1]+b13*velvec[2]; /* Velocity components in face oriented coordinate system */
```

```
                        tvel1=b21*velvec[0]+b22*velvec[1]+b23*velvec[2];
                        tvel2=b31*velvec[0]+b32*velvec[1]+b33*velvec[2];
                        ginner=pow(F_VOF(faceidentifier,sandthread)/0.63,0.333);
                        gzero=pow(1-ginner,-1);                 /* The radial distribution function */

            granvisk=F_VOF(faceidentifier,sandthread)*diam*rhos*sqrt(3.1415*F_GT(faceidentifier,sandthread))*(1+2*(1+rescof)*(3*rescof-
1)*F_VOF(faceidentifier,sandthread)*gzero/5)/6/(3-rescof); /* Syamlal-obrian viscosity relaion */

            granvisk2=F_VOF(faceidentifier,sandthread)*diam*rhos*sqrt(3.1415*F_GT(faceidentifier,sandthread))*(1+2*(1+rescof)*(3*rescof-
1)*F_VOF(faceidentifier,sandthread)*gzero/5)/6/(3-rescof);
                        if (zone_ID==7 && granvisk<=lim && limit1==1)
                        {
                        limit1=2;
                        Message("granvisk low = %g lambdap = %g\n",granvisk2,granvisk);
                        }
                        if (granvisk>=lim)
                        {
                        granvisk=lim;
                        limit3=2;
                        }
                        lambdap=sqrt(3*3.1415)*diam/24/F_VOF(faceidentifier,sandthread)/gzero;
                        if (limit3==2 && limit2==3)
                        {
                        Message("granvisk = %g lambdap = %g\n",granvisk2,granvisk);
                        limit3=3;
                        limit2=2;
                        }
                        nshear=0;  /* Calculate shear components */
                        tshear1=tvel1*granvisk/lambdap;
                        tshear2=tvel2*granvisk/lambdap;
                        shearx=a11*nshear+a12*tshear1+a13*tshear2;
                        sheary=a21*nshear+a22*tshear1+a23*tshear2;
                        shearz=a31*nshear+a32*tshear1+a33*tshear2;
                        F_PROFILE(faceidentifier,sandthread,index)=1*shearx;    /* Set the shear x component */
                        #endif
            }
end_f_loop(f,thread)
}
```

Appendix 2 Eulerian erosive wear model UDF

The following C++ script implements the erosive wear model of Lyckowsksi into ANSYS Fluent 14.0. The code is intended both for serial and parallel usage.

```
#include "udf.h"
#include "mem.h"
#include "surf.h"
#include "metric.h"
DEFINE_ON_DEMAND(erosionrate)
{
	real velu, velv, velw, velmag, grantemp, volfrac, afunc, bfunc, cfunc;
	real dens =7800;
	real dens2 =2560;
	real k =0.000000002;
	int zone_ID=8;
	Thread *sandthreadweld;
	Domain *sanddomain;
	face_t faceidentifier;
	sanddomain=Get_Domain(3);
	sandthreadweld=Lookup_Thread(sanddomain,zone_ID);
	begin_f_loop(faceidentifier,sandthreadweld)
	if PRINCIPAL_FACE_P(faceidentifier,sandthreadweld)
	{
		#if !RP_HOST
		velu=F_U(faceidentifier,sandthreadweld);
		velv=F_V(faceidentifier,sandthreadweld);
		velw=F_W(faceidentifier,sandthreadweld);
		velmag=sqrt(pow(velu,2)+pow(velv,2)+pow(velw,2));
		grantemp=F_GT(faceidentifier,sandthreadweld);
		volfrac=F_VOF(faceidentifier,sandthreadweld);
		afunc=0.1*pow(2*grantemp,1.5)/sqrt(3.14159265);
		bfunc=0.05*pow(velmag,2)*sqrt(2*grantemp/3.14159265);
		cfunc=0.09*velmag*grantemp;

	F_UDSI(faceidentifier,sandthreadweld,0)=75*31500000000*k*volfrac*dens2*pow(velmag,0.6)*(afunc+bfunc+cfunc)/dens/3200;
		#endif
	}
	end_f_loop(faceidentifier,sandthreadweld)
}
```

Appendix 3 Lagrangian simulation results

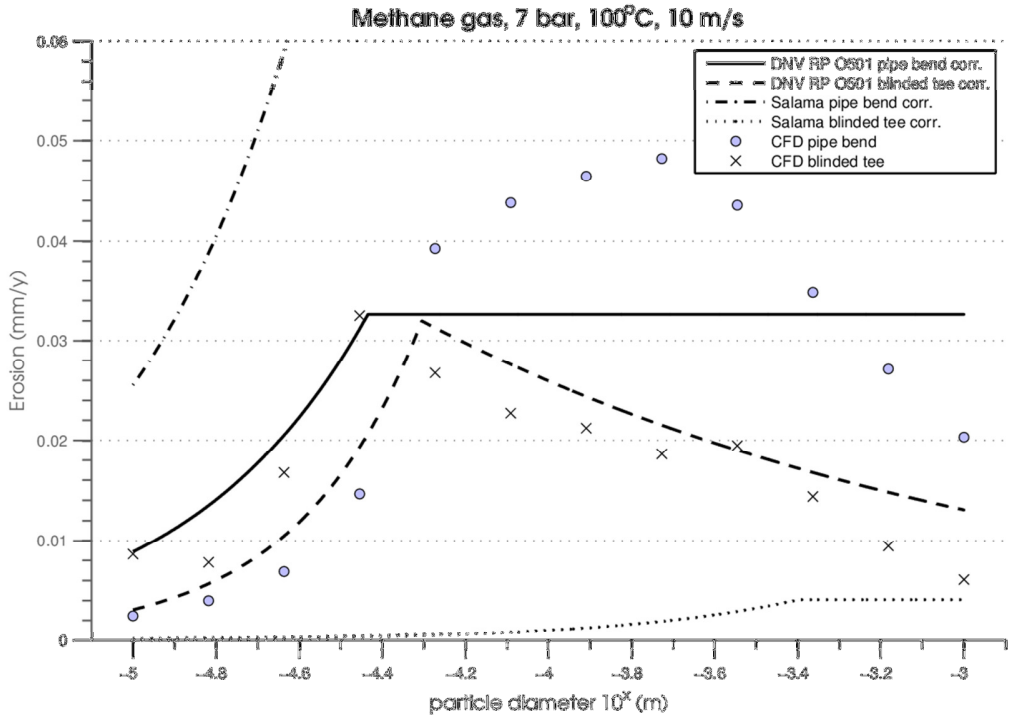

Fig. 22: Maximum erosion rate versus particle size at 10 m/s.

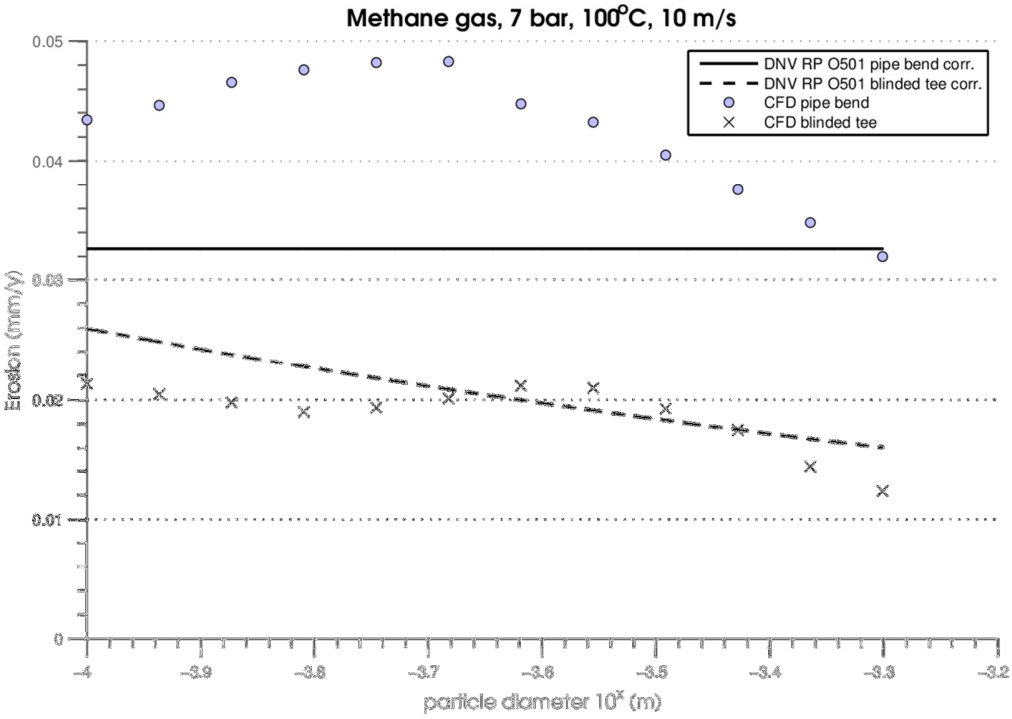

Fig. 23: Maximum erosion rate versus particle size at 10 m/s.

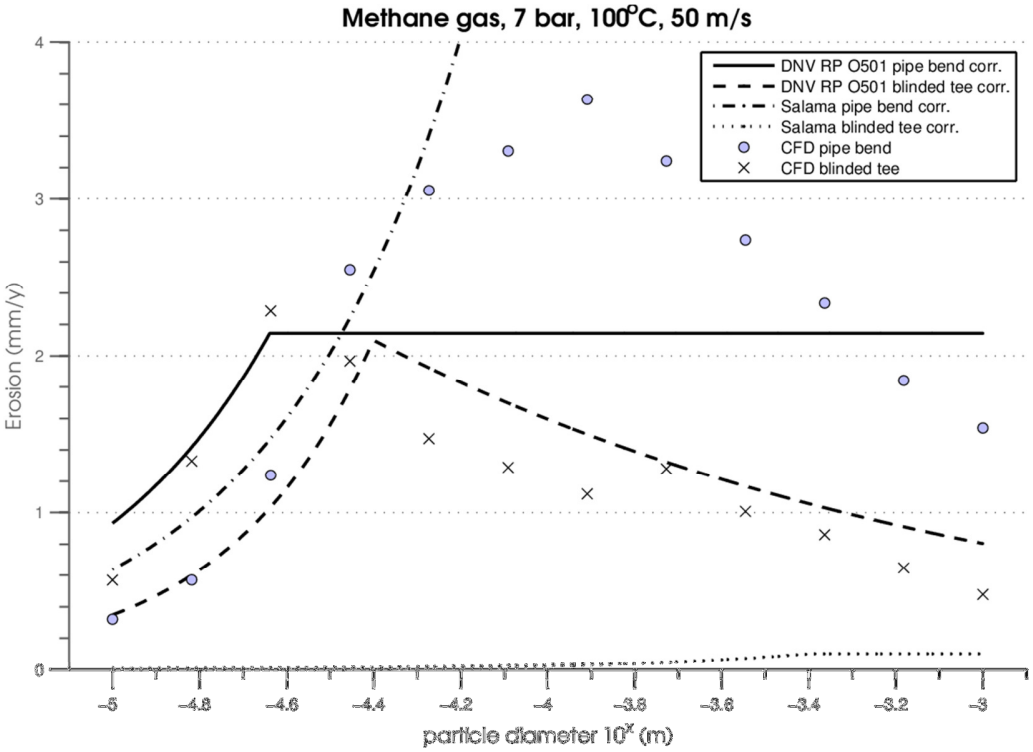

Fig. 24: Maximum erosion rate versus particle size at 50 m/s.

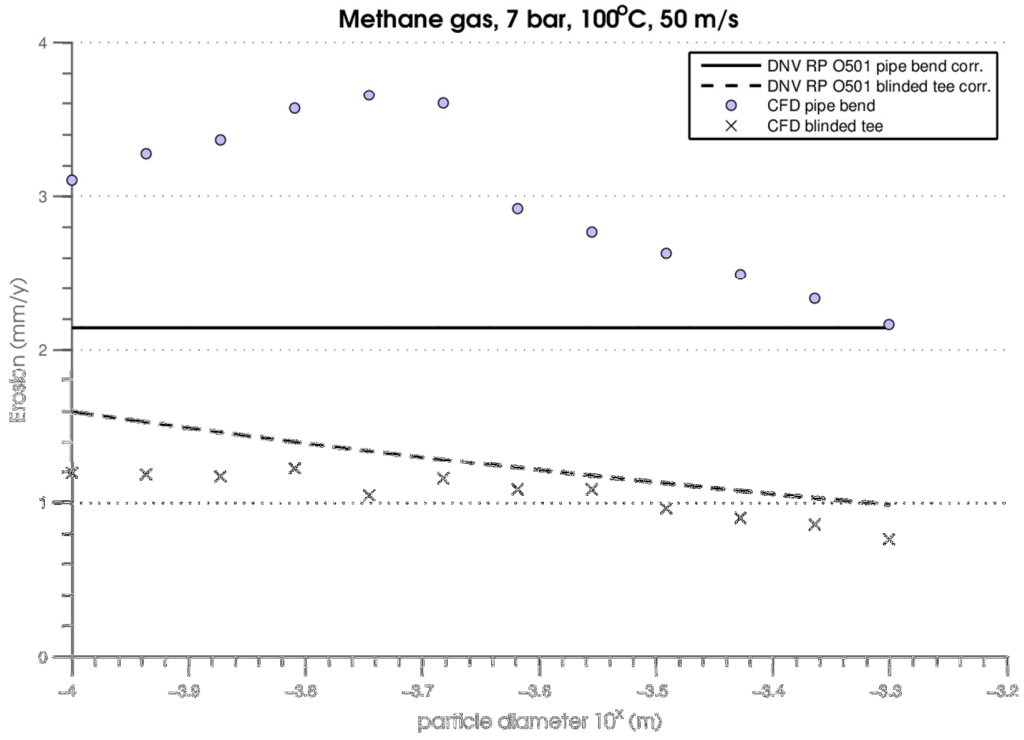

Fig. 25: Maximum erosion rate versus particle size at 50 m/s.

Appendix 4 Case settings and simulation input

General data

The material data for all materials used are presented below.

Table 2: Density and viscosity used throughout simulations

Air	**Sand**
Density: 1.225 kg/m^3	Density: 2600 kg/m^3
Viscosity: 1.7894e-5 kg/ms	**Steel**
Natural gas	Density: 7800 kg/m^3
Density: 4.82 kg/m^3	**Aluminum**
Viscosity: 1.1e-5 kg/ms	Density: 2719kg/m^3

Eulerian-Lagrangian simulations

Particle size effect:

Fluid type: Methane
Geometry: Pipe bend, blinded tee
Pipe diameter: 100 mm
Diameter range 1: 10 15 23 35 53 81 123 187 284 432 657 1000 micron
Diameter range 2: 100 115 134 155 180 207 240 278 322 373 432 500 micron
Case 1 – 48 (inlet velocity 1 m/s)
Case 49 – 96 (inlet velocity 10 m/s)
Case 96 – 144 (inlet velocity 50 m/s)
Mass flow sand: 0.25 kg/s

Fluid type: Air
Identical simulations as for methane except that only diameter range 1 was carried out, in total 72 cases.

Velocity series:

Fluid type: Methane
Geometry: Pipe bend
Particle diameter: 500 μm
Pipe diameter: 100 mm
Velocity: 1 m/s, 2 m/s, 5 m/s, 10 m/s, 15 m/s, 25 m/s, 35 m/s, 50 m/s
Mass flow sand: 0.25 kg/s

Pipe diameter variation:

Fluid type: Methane
Geometry: Pipe bend
Particle diameter: 240 μm
Pipe diameter: 40 mm, 60mm, 80mm, 100mm
Mass flow sand: 0.25 kg/s

Experimental set validation:
Fluid type: Air
Particle diameter: 223 microns
Pipe diameter: 101 mm, for other dimensions see table X
Flow velocity: 80 m/s
Sand mass: 5 runs in 50 kg increments

Eulerian-Eulerian simulations

Particle size effect:
Fluid type: Air
Geometry: Pipe bend
Pipe diameter: 100 mm
Diameter range: 250, 300, 350, 400, 450, 500 μm
Loading: 0.0123

Velocity series:
Fluid type: Air
Geometry: Pipe bend
Particle diameter: 500 μm
Pipe diameter: 100 mm
Velocity: 1 m/s, 1.5

Appendix 5 Geometry data

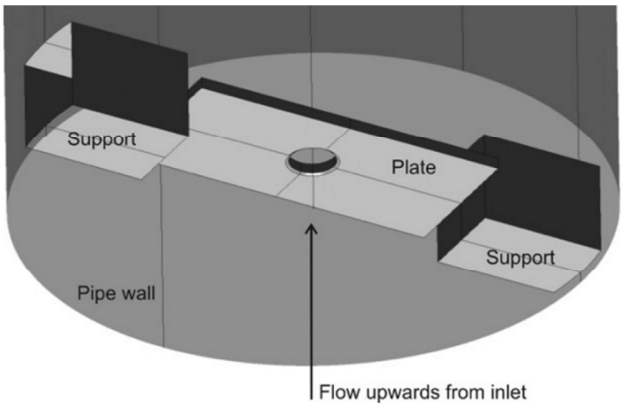

Fig. 26: Plate with hole through center point fixed via support at the inner pipe wall. Sand travelling through the pie will impact plate and due to the hole in plate center deviate from straight trajectories before impact.

Table 3: Geometry dimensions

	(mm)
Inlet length	3000
Outlet length	1000
Diameter	101
Hole radius	4
Plate	
Height	24
Thickness	2
Width	50
Support block	
Height	16
Thickness	12
Width	25.5

Table X: Geometry dimensions for pipe bend

	(mm)
Inlet length	1000
Outlet length	500
Diameter	100
Curvature	1.5

Table X: Geometry dimensions for (mm)

Blinded tee	
Inlet length	1000
Outlet length	500
Diameter	100
Blind depth	5